DOE/MC/10514-T1

DOE/MC/10514-T1

FOSSIL ENERGY

HYDRAULIC FRACTURING AND ASSOCIATED STRESS MODELING FOR THE EASTERN GAS SHALES PROJECT

Final Report, April 1, 1979—November 15, 1980

By
Sunder H. Advani

November 1980

Work Performed Under Contract No. AC21-79MC10514

Department of Engineering Mechanics
College of Engineering
The Ohio State University
Columbus, Ohio

U. S. DEPARTMENT OF ENERGY

DOE/MC/10514-T1
Distribution Category UC-92a

HYDRAULIC FRACTURING AND ASSOCIATED STRESS MODELING FOR THE EASTERN GAS SHALES PROJECT

Sunder H. Advani
Principal Investigator

Department of Engineering Mechanics
College of Engineering
The Ohio State University
Columbus, Ohio 43210

FINAL REPORT: April 1, 1979 to November 15, 1980

Prepared for the Morgantown Energy Technology Center
U.S. Department of Energy
Under Contract No. DE-AC21-79MC10514

TABLE OF CONTENTS

FOREWORD

This report describes the work performed under U.S.D.O.E. contract No. DE-AC21-79MC10514 with the Ohio State University for the period April 1, 1979 to November 15, 1980. The work details hydraulic fracturing and associated stress modeling investigations for the Eastern Gas Shales Project (EGSP).

Dr. Sunder H. Advani served as Principal Investigator for the project with contract monitoring by Mr. Charles A. Komar of the Morgantown Energy Technology Center. Contributions to this program were made by Mr. O. Gurdogan, Mr. E.Y. Lee. Mr. F-S. Hung, Mr. R. Stonesifer, and Mr. T. Irvine.

1.0 INTRODUCTION

The U.S. Department of Energy Enhanced Gas Recovery Program is currently focusing on four major targets for unconventional gas resources. These sources include:

(i) Tight Gas Sands

(ii) Eastern Gas Shales

(iii) Methane from Coal Beds

(iv) Geopressured Aquifers

It is anticipated that the unconventional gas resources can provide a healthy increment of energy in the short and mid-term with potential production of 5-8 TCF/year by 1990. In particular, the Eastern Gas Shales Project (EGSP) is developing optimum methods and supporting rationale for stimulating gas production from the Eastern petroliferous basins with primary emphasis on the Devonian shales. The phenomenological theories for gas production from these Devonian shales are, to a large degree, based on (i) the frequency, extent, and preferred orientations of fracture and joint systems, and (ii) the thickness, maturation, and source richness of the black shales. The role of natural fracture systems as communication channels for the free, readily releasable and absorbed gas has been discussed by several investigators. The extent and orientation of the natural fracture systems and joints is a function of complex geomechanical relationships such as basement-sedimentary cover interactions, in situ stress gradients, and anisotropies. To fully exploit these fracture systems, optimum stimulation treatments (i.e., hydraulic fracturing, explosive fracturing) based on defined reservoir properties and production objectives

have to be defined. The choice of the appropriate stimulation treatment, say hydraulic foam fracturing, is therefore a multivariable function of reservoir and rock mechanics parameters.

This report details hydraulic fracture and associated stress modeling investigations for the EGSP. A review of pertinent literature along with model formulations, results, and applications associated with the developed hydraulic fracture model are given. Examples relating to foam fracture and dendritic fracture modeling are also provided. Supplementary information is detailed in the appendices. The primary objective of this report is to provide predictive and interpretive insight for hydraulic fracture mechanisms and design. Additionally, it is hoped that this report will serve as an updated extension of the hydraulic fracturing monographs written by Howard and Fast [1] and Halliburton [2].

2.0 LITERATURE REVIEW

The earliest rigorous effort on hydraulic fracture modeling is due to Zheltov and Kristianovitch [3]. Subsequent investigations by Perkins and Kern [4], Haimson and Fairhurst [5], Nordgren [6], Geertsma and De Klerk [7], and Daneshy [8] have examined special features such as fracture width and extent determination, fracture initiation and propagation, and fracture design based on simplified fluid flow and linear isotropic elasticity theory models. These models and related assumptions have been recently reviewed by Geertsma and Haafkens [9] along with fracture geometry comparisons for the various theories.

The use of finite element models for the evaluation of stresses and stress intensity factors induced in hydraulic fracturing has been introduced by Advani et al [10,11] and Shuck and Advani [12]. Incorporation of the effects of elasto-diffusive coupling for studying hydraulic fracture mechanisms is due to Rice and Cleary [13] and Ruina [14]. Models including the effects of multi-layering have been studied by Daneshy [15], Simonsen et al [16], Advani et al [17], Cleary [18] and Hanson et al [19]. Sophisticated codes specifically applicable to vertical hydraulic fracturing design have been recently developed by Advani et al [20], Terra Tek [21], and Hanson et al [22]. The growth of planar cracks induced by hydraulic fracturing has been recently studied by Mastrojannis et al [23].

Various Devonian shale field experiments have been conducted by industry under DOE sponsorship [24, 25, 26]. Mine back fracturing experiments are presently being conducted by Sandia Laboratories [27] and laboratory experiments are in progress at Lawrence Livermore Laboratory [28] and Stanford

Research International [29]. These experiments with the supportive computer codes are providing rationale for stimulation design. In this context, preliminary design rationale for Devonian shale experiments has been presented by Komar [30]. Interpretation of field fracturing pressures and determination of frature parameters from fracturing pressure decline curves enhance knowledge of the in situ stress fields and fracture growth [31,32].

Recent research related to proppant transport has been reported by Novotny [33] and Daneshy [34]. A simplified form of the proppant transport equation has been incorporated by Settari and Price [35] in their hydraulic fracturing model.

3.0 HYDRAULIC FRACTURE MODEL FORMULATIONS AND RESULTS

A general schematic of the hydraulic fracture model for various time steps is illustrated in Figure 1 with the vertical fracture residing primarily in the pay zone. The fracture configuration suggests a three dimensional analysis for the fluid flow and structural response analysis. However, in view of the laborious coding and computational costs for three dimensional models, simplified two dimensional models can be initially examined. Figure 2 illustrates an octant of the selected three dimensional finite element vertical crack model. Stress intensity factors and field stress magnitudes associated with this model for constant fracture height and uniform crack pressure have been previously reported [36]. Figure 3a reveals the half width profile in the vertical plane at different cross-sections designated by the value of x/H. As expected, the profile at x/H = 0 approaches the plane strain case. Figure 3b illustrates the width profile in the horizontal symmetry plane for this model. These results indicate that the three dimensional width profile has an ellipsoidal form and that for large fracture horizontal extent to height ratios, the plane strain structural approximation generally yields accurate results for the width profile. Similar correlations for the crack stress intensity factors and field stress magnitudes have also been obtained. Therefore, the width analysis presents results for idealized two dimensional hydraulic fracture models which represent a vertical cross-section of the fracture.

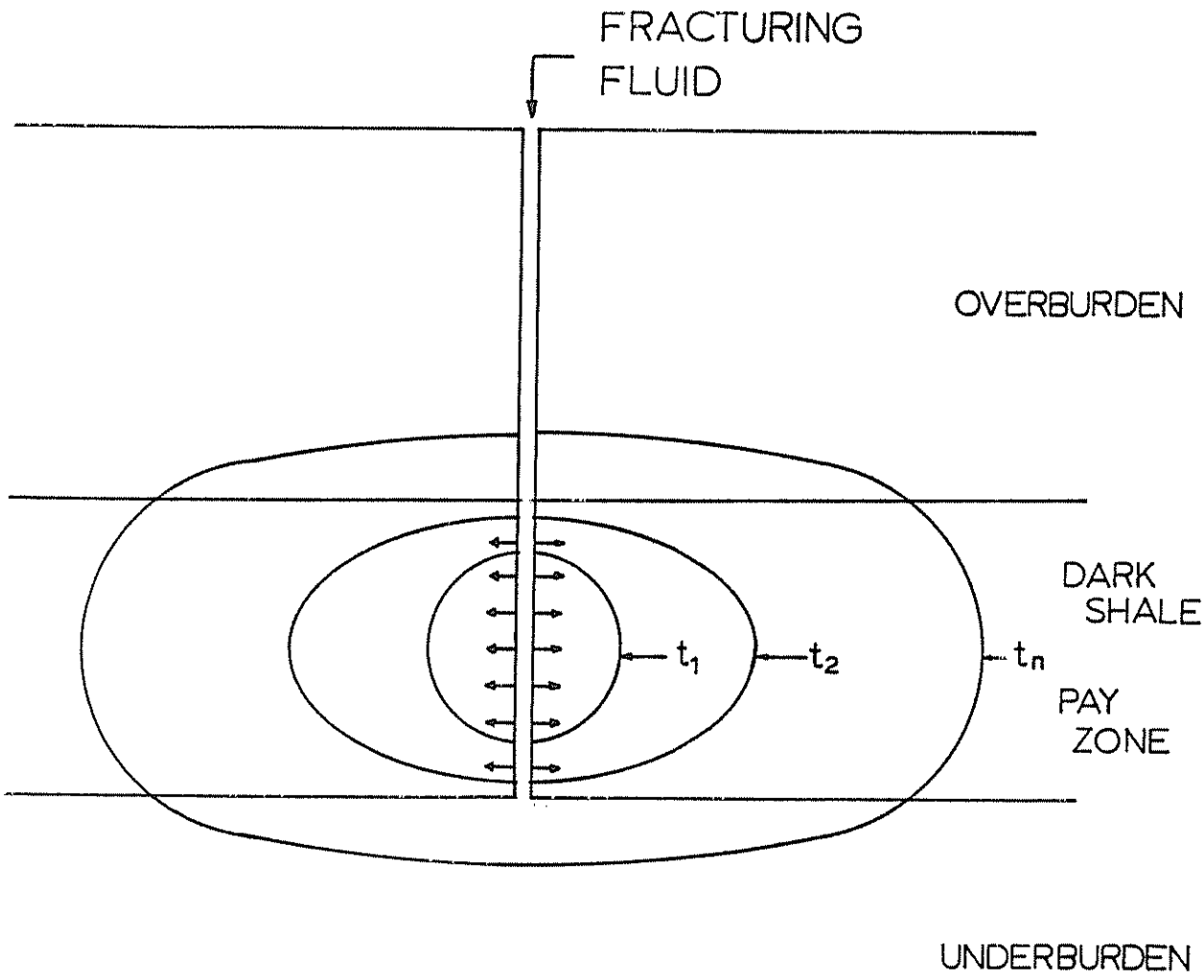

Figure 1: Schematic of Vertical Hydraulic Fracture Geometry for Different Time Steps.

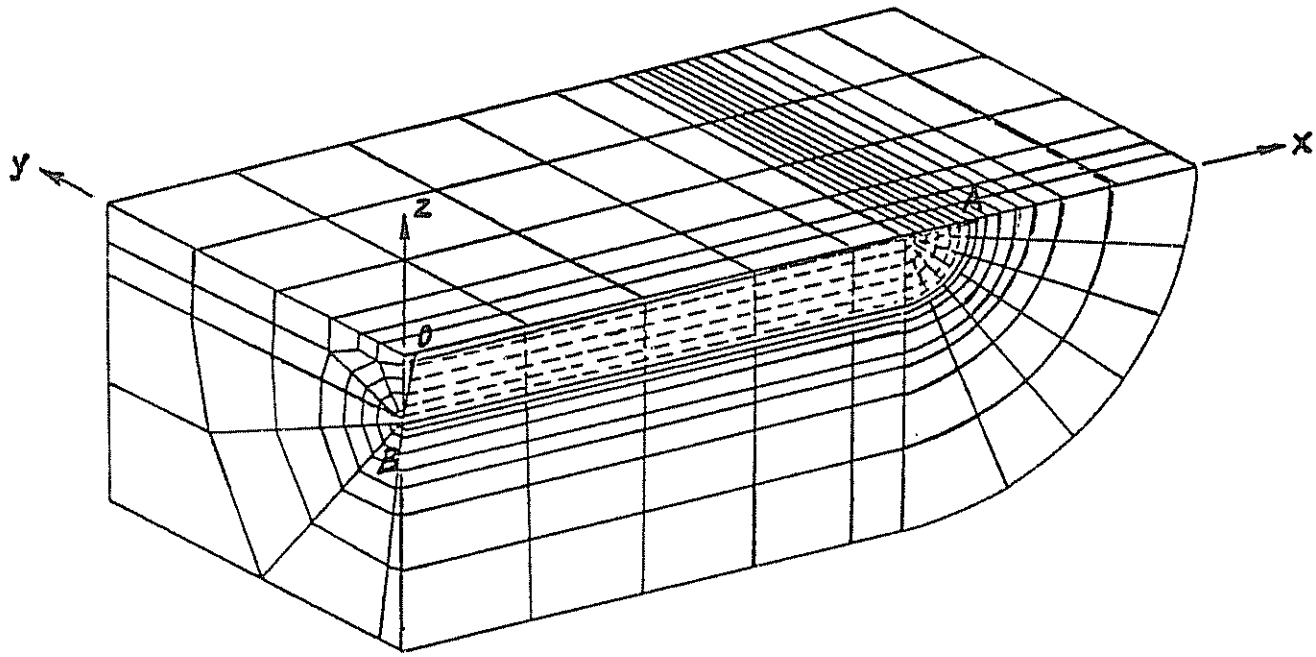

Figure 2: Octant of Three Dimensional Finite Element Model with Crack (OAB).

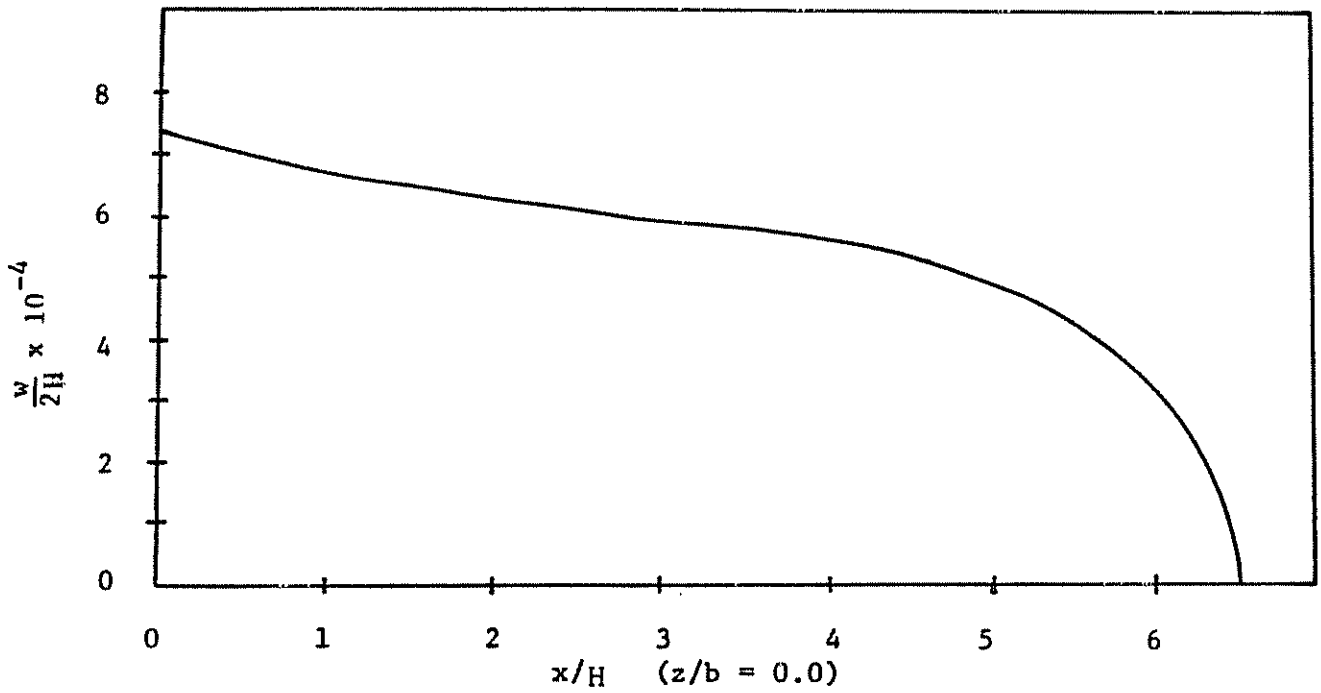

Figure 3a: Width Profile for 3D Model along x axis for z = 0.

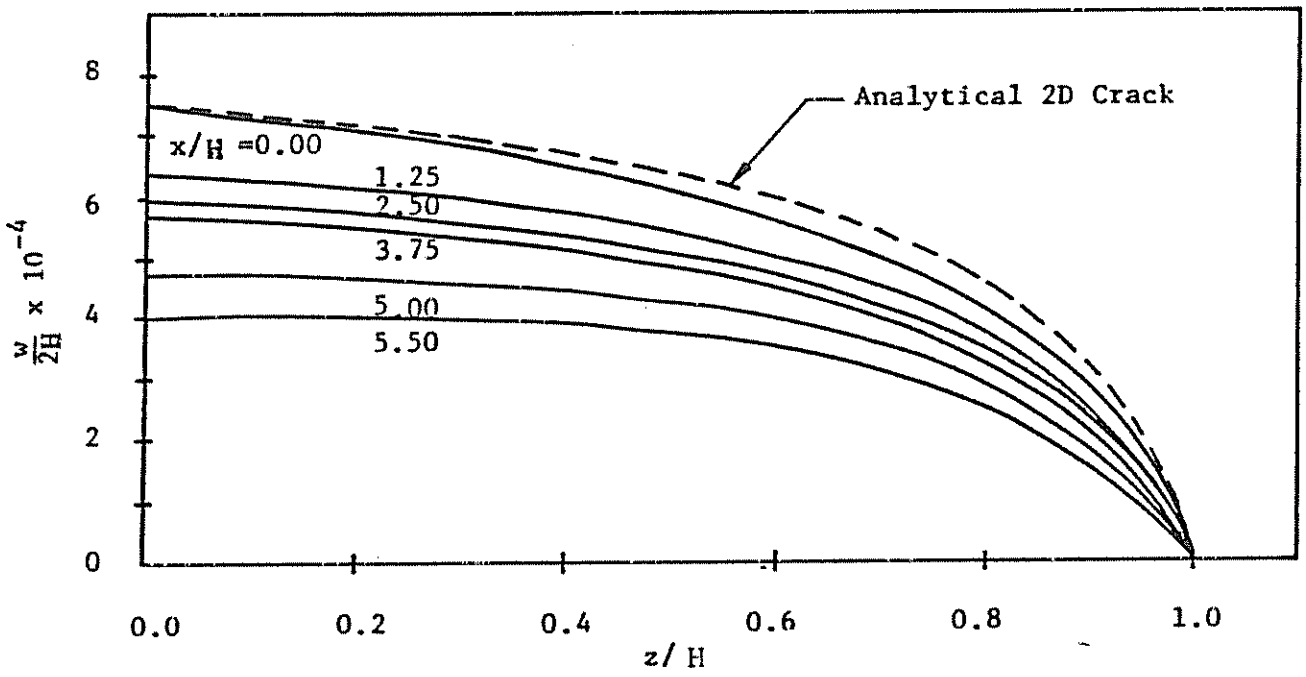

Figure 3b: Width Profile for 3D Model along z axis at Different Vertical Sections.

3.1 Plane Strain Hydraulic Fracture Model

The selected plane strain vertical crack model is illustrated in Figure 4 with fluid coupling provided by the crack interface pressure. The vertical width profile for the isotropic elastic model with uniform in situ stress perpendicular to the fracture plane is elliptical in shape. The maximum width W(x,t), in this case, is governed by

$$W(x,t) = \frac{4(1-\nu^2)\ H\ \Delta p}{E} \tag{1}$$

where $\Delta p = p - \sigma_{H\ MIN}$

The average fracture width obtained by integrating the vertical fracture width variation is

$$\overline{W}(x,t) = \frac{\pi(1-\nu^2)\ H\ \Delta p}{E} \tag{2}$$

If the horizontal cross-section is considered instead, the quantity H in the above expressions can be approximately replaced by the fracture half length L.

For the layered case, illustrated in Figure 4, the selected finite element model represented by a quadrant is illustrated in Figure 5. Figures 6a and 6b reveal the computed average fracture widths for different ratios of H/h and E_2/E_1 for frac fluid and differential tectonic loading respectively. Different cases can be superposed to yield width magnitudes for various loadings, material property ratios, and fracture geometries. The corresponding fracture height is obtained by computing the stress

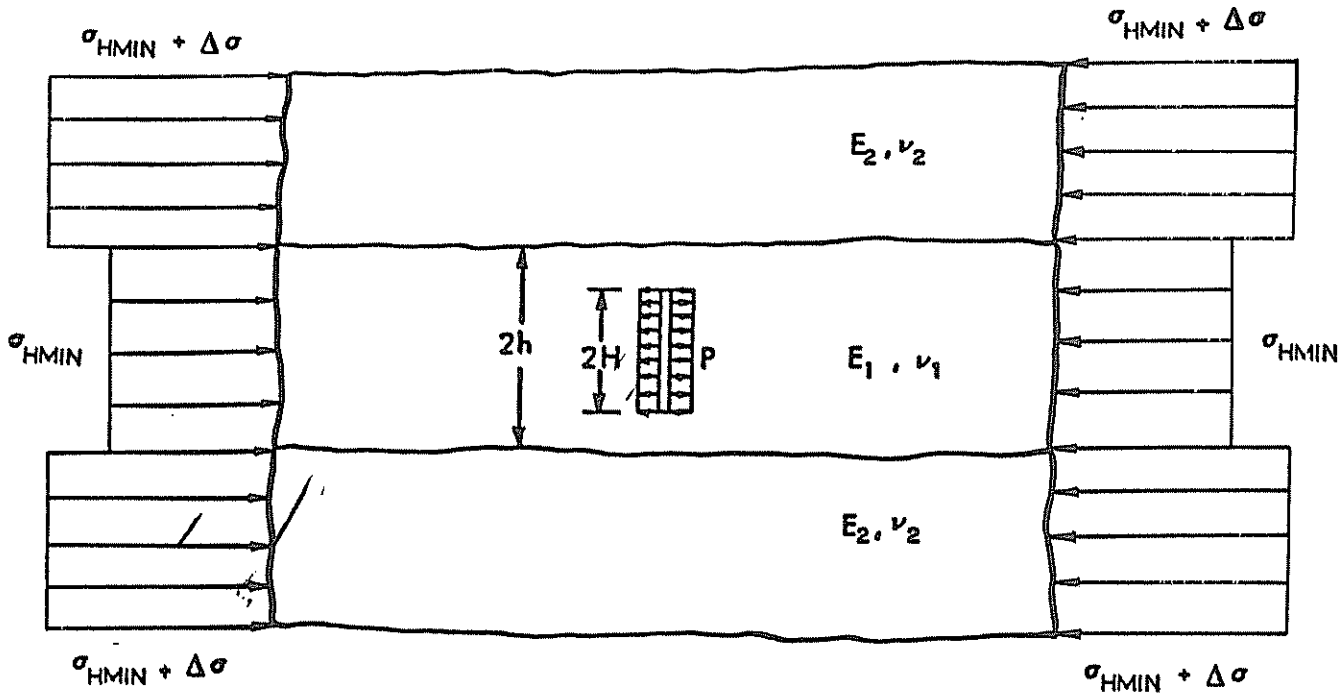

Figure 4: Plane Strain Layered Vertical Crack Model with Induced Pressure and Tectonic Loading.

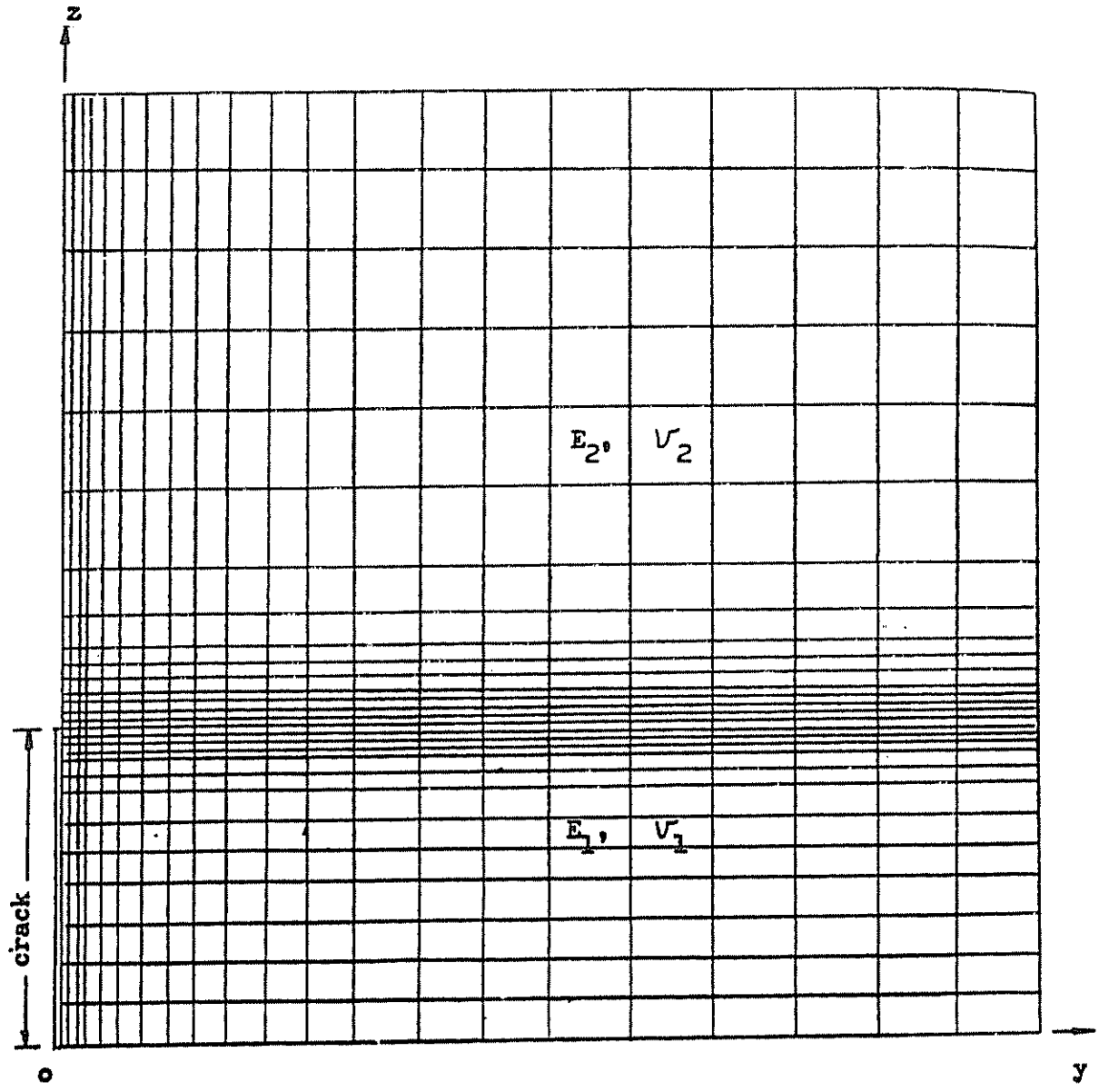

Figure 5: Two Dimensional Finite Element Mesh for Model in Figure 4.

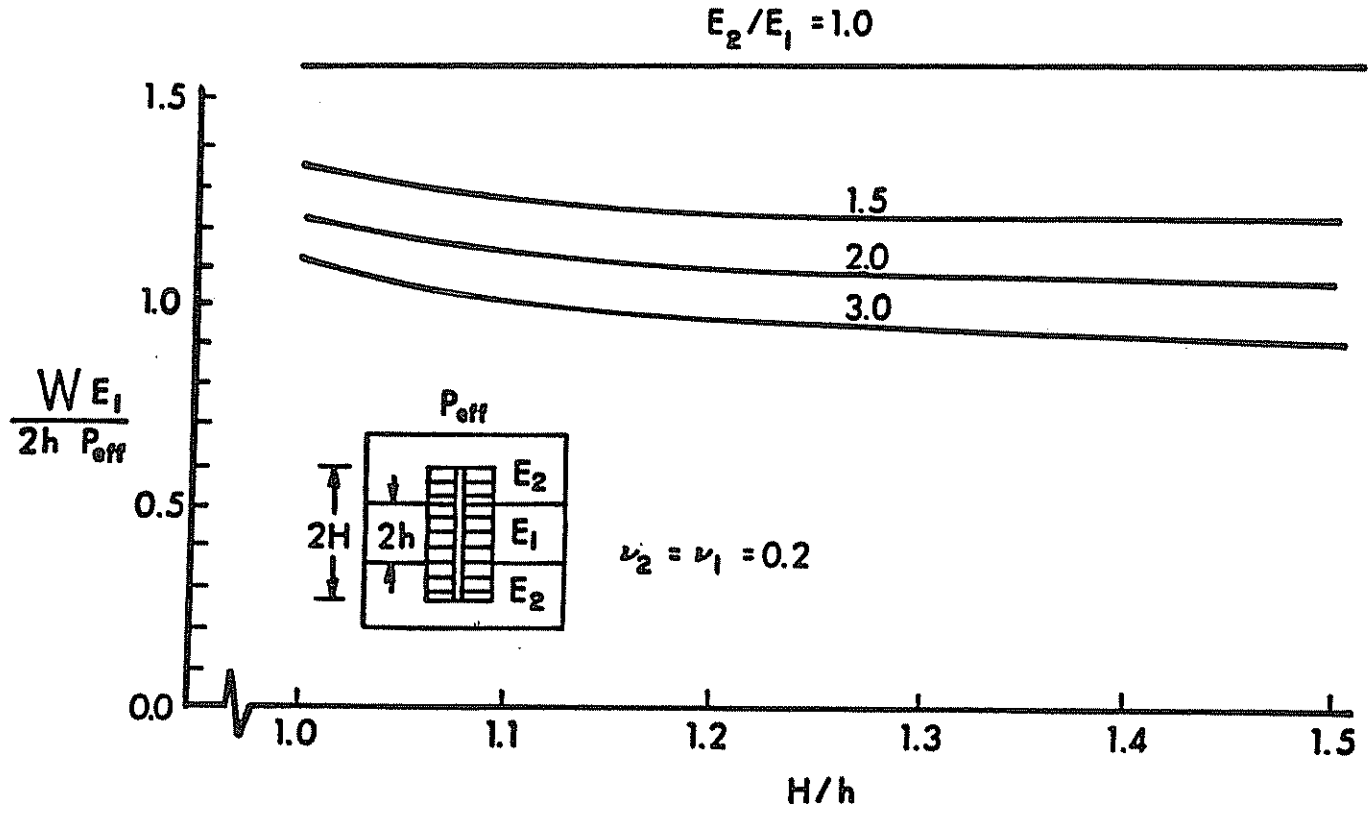

Figure 6a: Computed Average Fracture Width Magnitudes Induced by Pressure Loading for Different E_2/E_1.

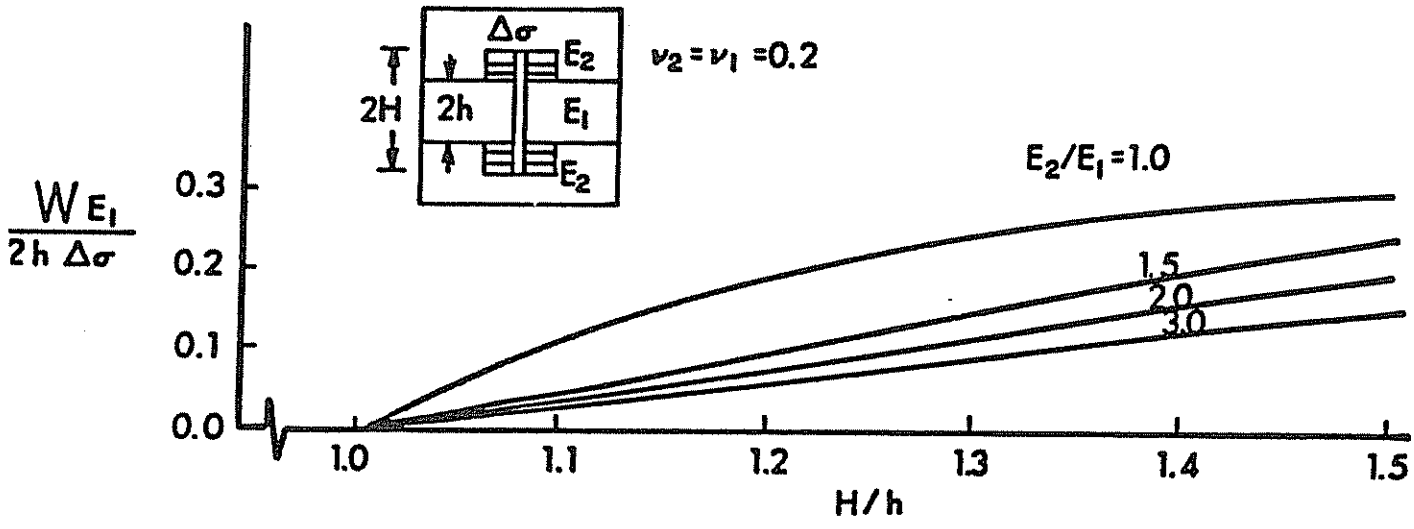

Figure 6b: Computed Average Fracture Width Magnitudes Induced by Differential Tectonic Loading for Different E_2/E_1.

intensity factors associated with the frac fluid pressure (Figure 7a) and tectonic loading (Figure 7b). The fracture height penetration versus bottom hole treatment curves can then be developed from the results depicted in Figures 7a and 7b for specified values of E_2/E_1, fracture toughness for the layers, and differential tectonic stress (Figures 8,9).

3.2 Fracturing Fluid Flow Simulations

Different forms of fracturing fluid simulations for the plane strain model represented by Figure 4 are reported here depending on the selected flow assumptions, governing equations, and solution techniques.

The first type of fluid flow simulation entails application of Bernoulli's equation with suitable viscous friction losses (governed by Reynold's number) in the vertical fracture and use of Darcy's flow equation for the formation. Detailed equations and computer programs for this simulation are presented in reference [37]. The model parameters associated with the analysis are defined by: pay zone thickness (2h), fracture height (2H), average fracture width ($\overline{W}$), bottom hole treatment pressure (P), formation pore pressure (p_o), injection flow rate (Q), fracture cross-sectional area (A), formation permeability to fracturing fluids (k), fracturing fluid viscosity (μ), effective fluid compressibility (c), and minimum horizontal stress ($\sigma_{H\ MIN}$). Two basic conditions, namely the conservation of mass and no back flow condition are employed in the finite difference formulations. The total fluid volume is the sum of the fracture volume and the leak-off volume. The formation pore pressure, bottom hole treatment pressure, and fluid injection rate are assumed to be constant.

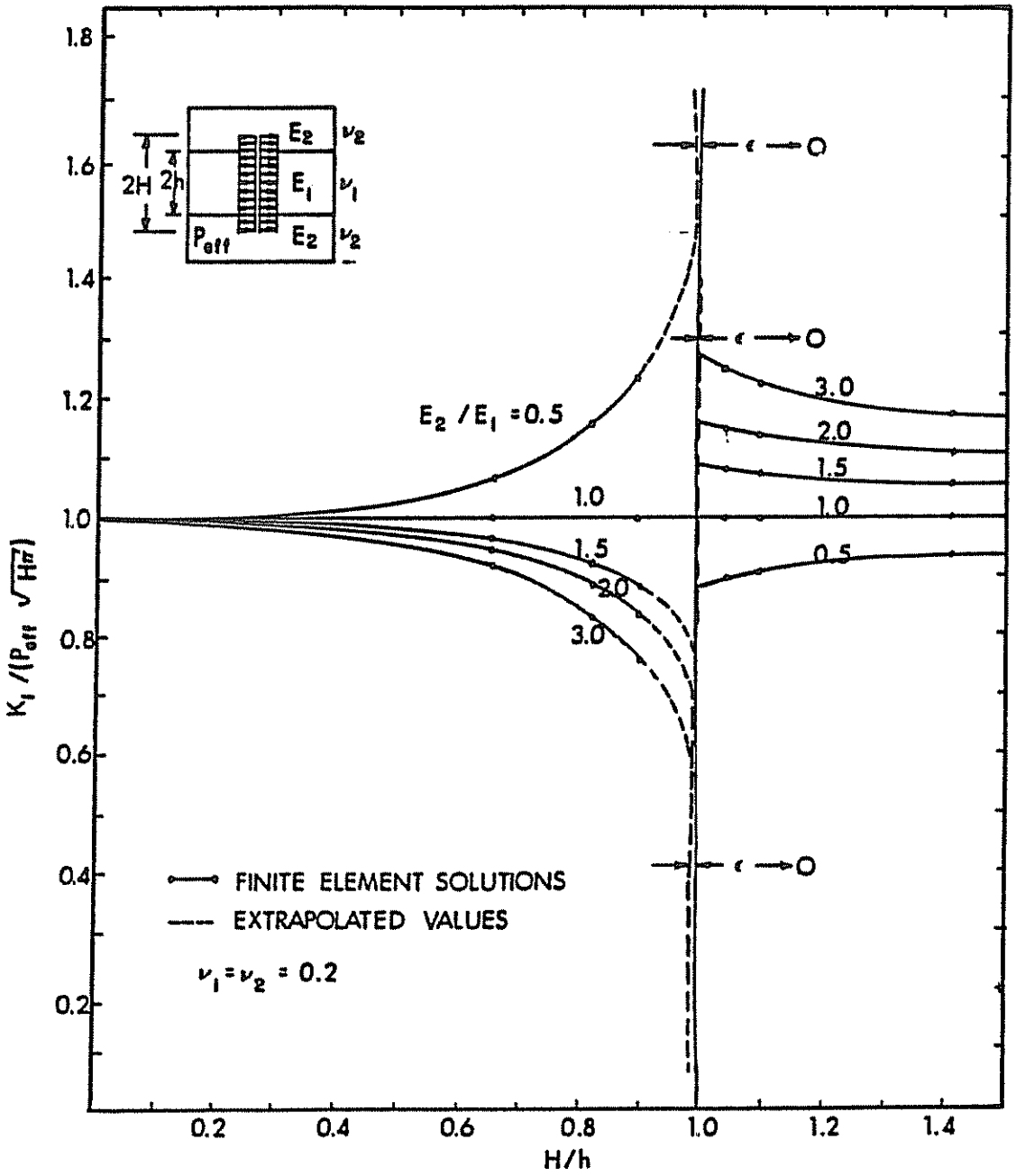

Figure 7a: Computed Stress Intensity Factors Induced by Crack Pressure Loading for Different E_2/E_1.

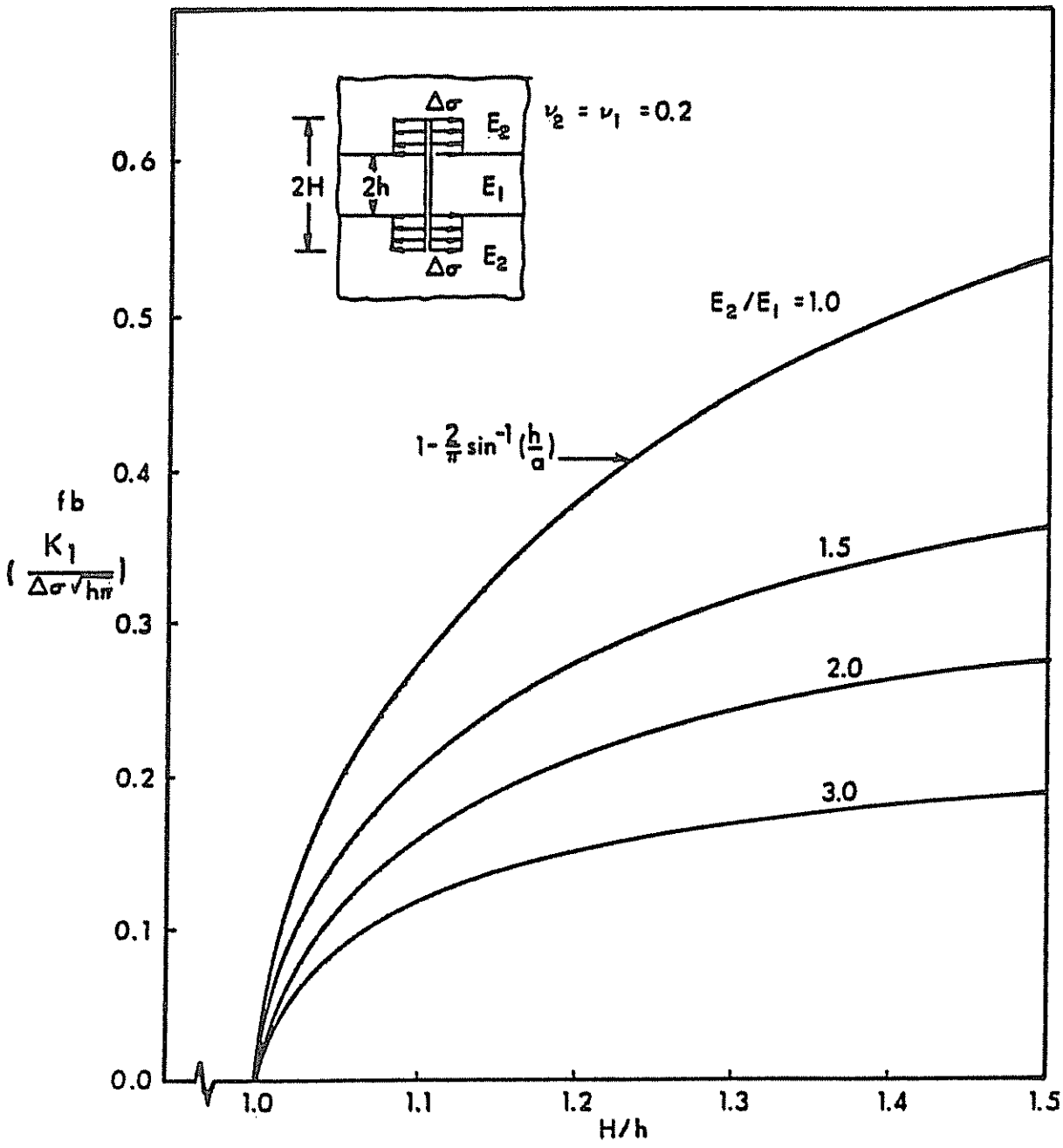

Figure 7b: Computed Stress Intensity Factors Induced by Differential Tectonic Loading for Different E_2/E_1.

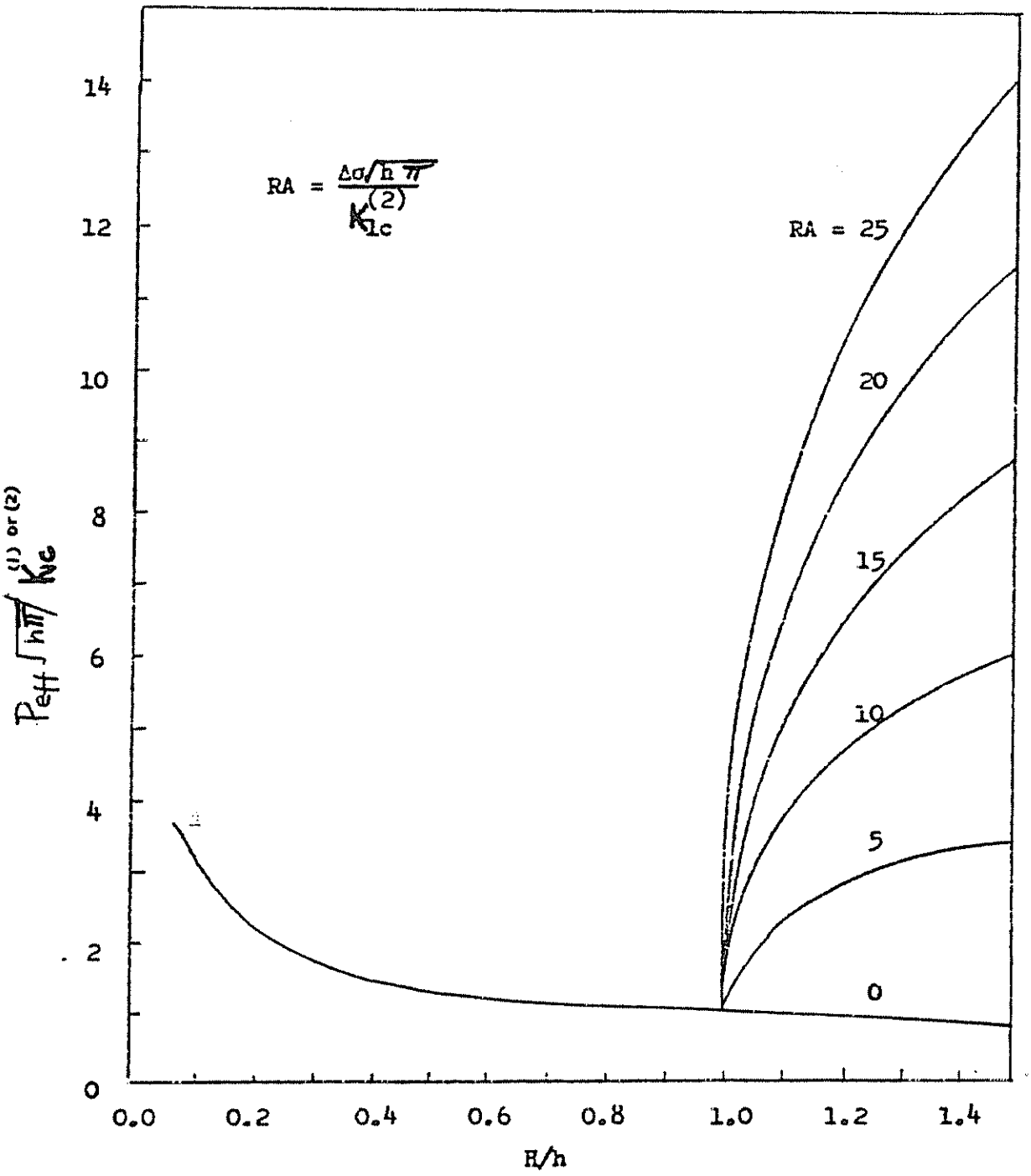

Figure 8: Effective Treatment Pressure ($P_{eff} = P_{BHTP} - \sigma_{HMIN}$) Versus H/h for $E_2/E_1 = 1$.

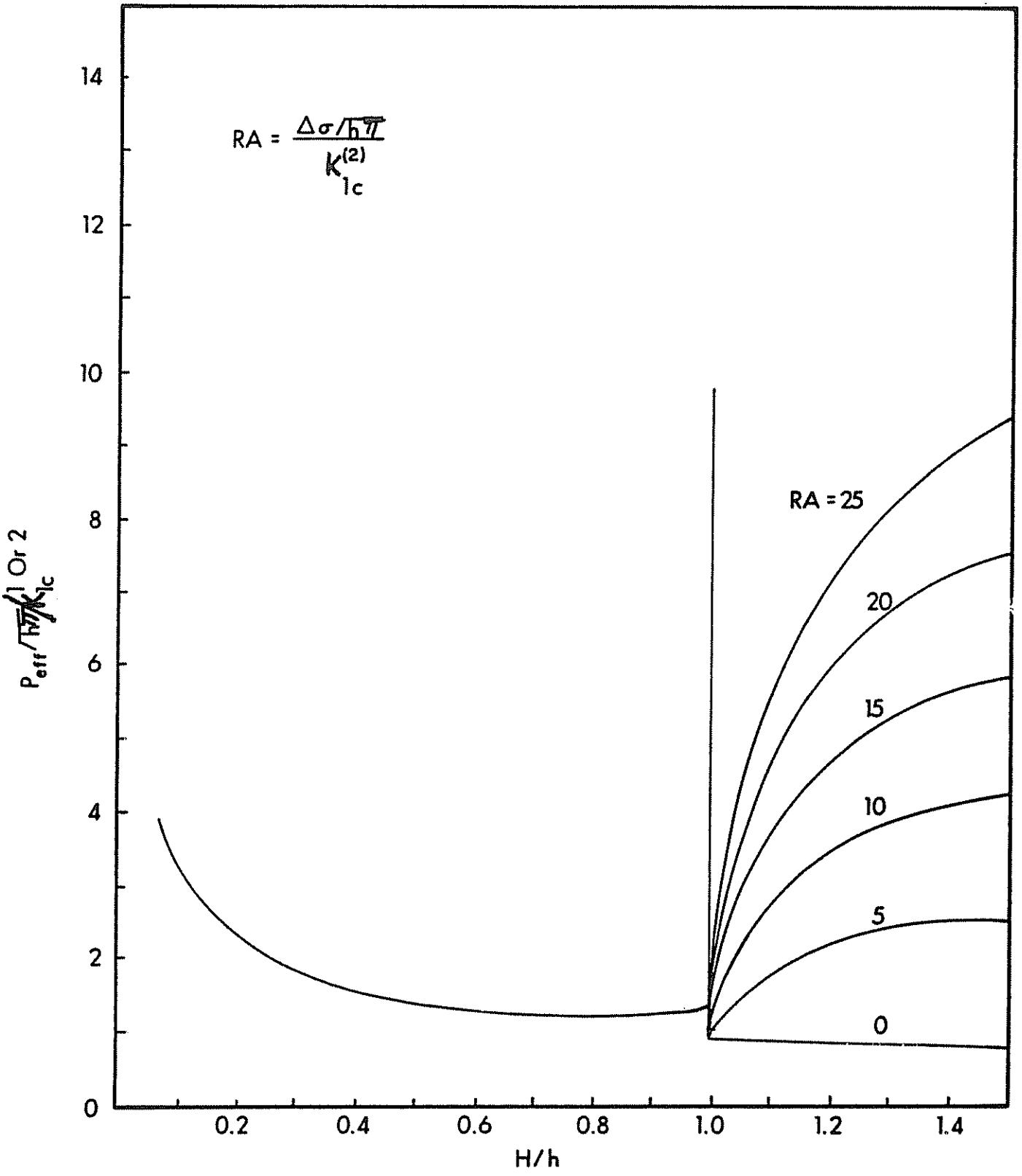

Figure 9: Effective Treatment Pressure ($P_{eff} = P_{BHTP} - \sigma_{HMIN}$) Versus H/h for $E_2/E_1 = 1.5$.

The iterative time step computations initially involve the determination of the total time duration for which each specified point on the fracture surface is exposed to the fracturing fluid with the cumulative leak-off effects included. Both incompressible and compressible fluids can be modeled.

The predicted fracture areas are based on the specified fracture width and computed fluid leak-off. Figures 10a,b, and c reveal the computed fracture areas for various flow indices or loss coefficients and fluid injection rates. Relative fracture areas for scaling to different fracture widths are illustrated in Figure 11. For specified reservoir conditions and treatment parameters, the flow index FI or loss coefficient is calculated from

$$FI = 0.00001913\ (k\phi\ \Delta P/\mu)^{\frac{1}{2}}\ ft/sec^{\frac{1}{2}}$$

for incompressible fluids

and

$$FI = 0.00001526\ (k\phi c/\mu)^{\frac{1}{2}}\ \Delta p\ ft/sec^{\frac{1}{2}}$$

for compressible fluids

where k is expressed in millidarcies, ϕ is the percentage porosity, μ is in centipoise (1/psi) units, c is the reciprocal of the bulk modulus and Δp is the effective bottom hole treatment pressure in psi. Alternatively, an overall fluid loss coefficient including the various effects such as static, viscous, and compression control loss coefficients can be used. Following specification of the loss coefficient, the fracture area corresponding to the prescribed injection rate and elapsed time can be obtained

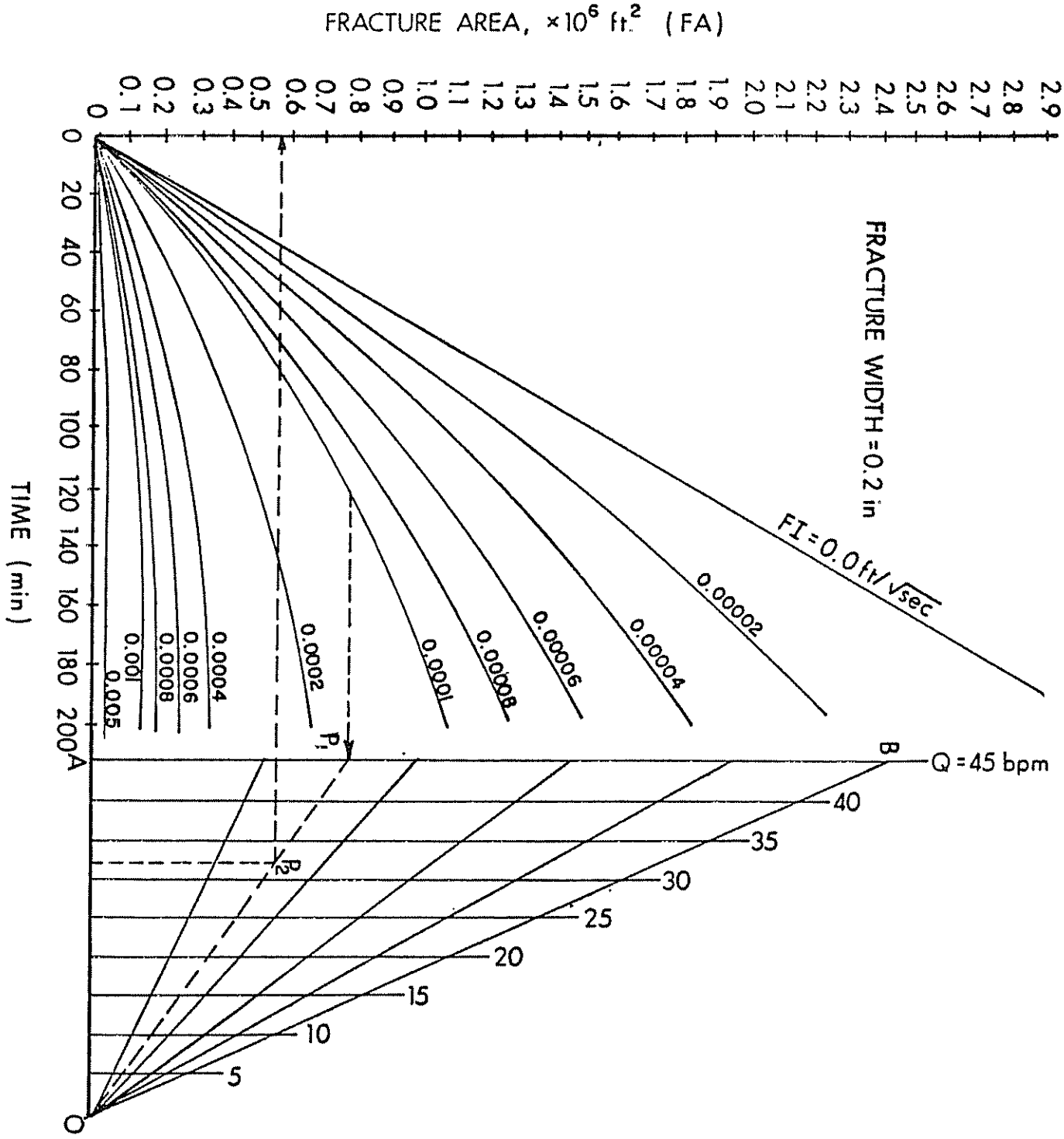

Figure 10a: Nomograph for Predicting Fracture Area for Specified Flow Rate, Treatment Time, and Flow Index (Width = 0.2 in).

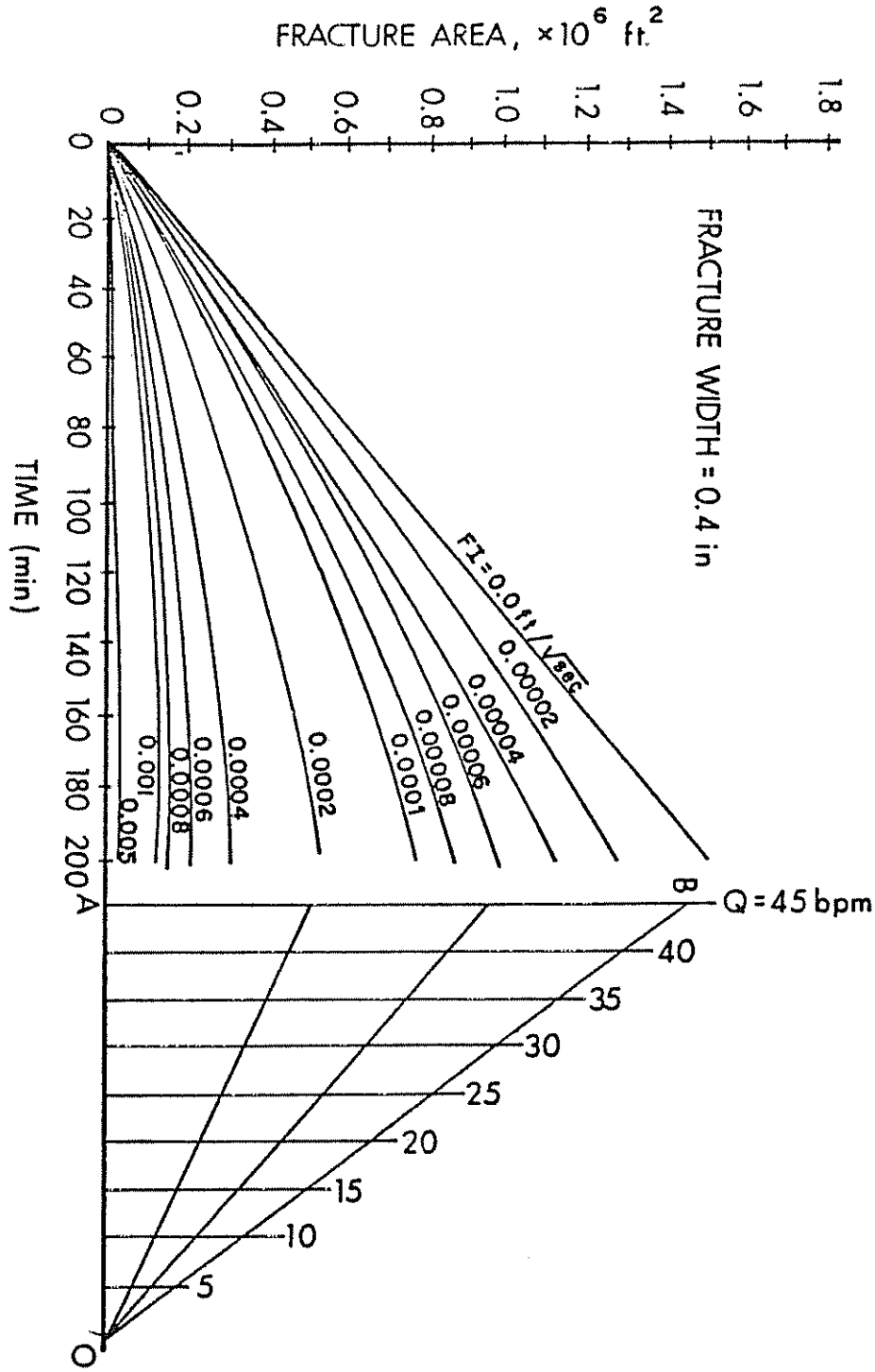

Figure 10b: Nomograph for Predicting Fracture Area for Specified Flow Rate, Treatment Time, and Flow Index (Width = 0.4 in).

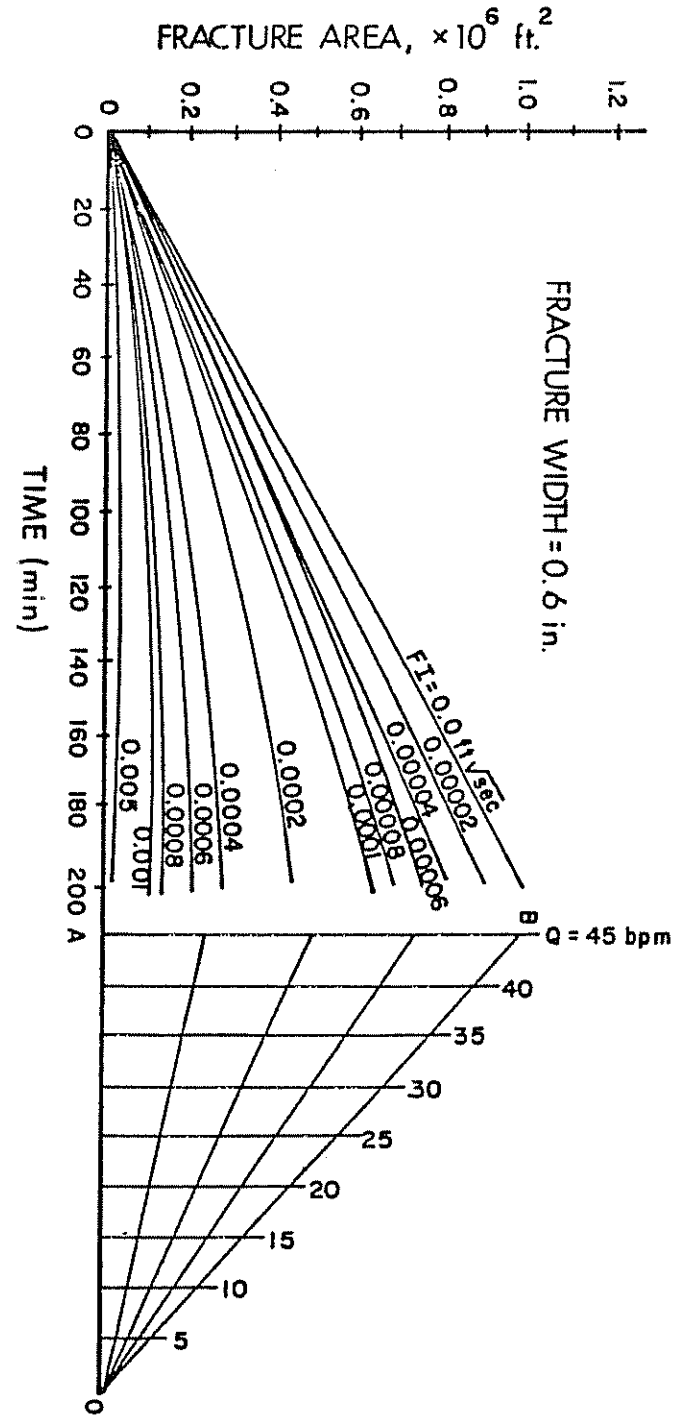

Figure 10c: Nomograph for Predicting Fracture Area for Specified Flow Rate, Treatment Time, and Flow Index (Width = 0.6 in).

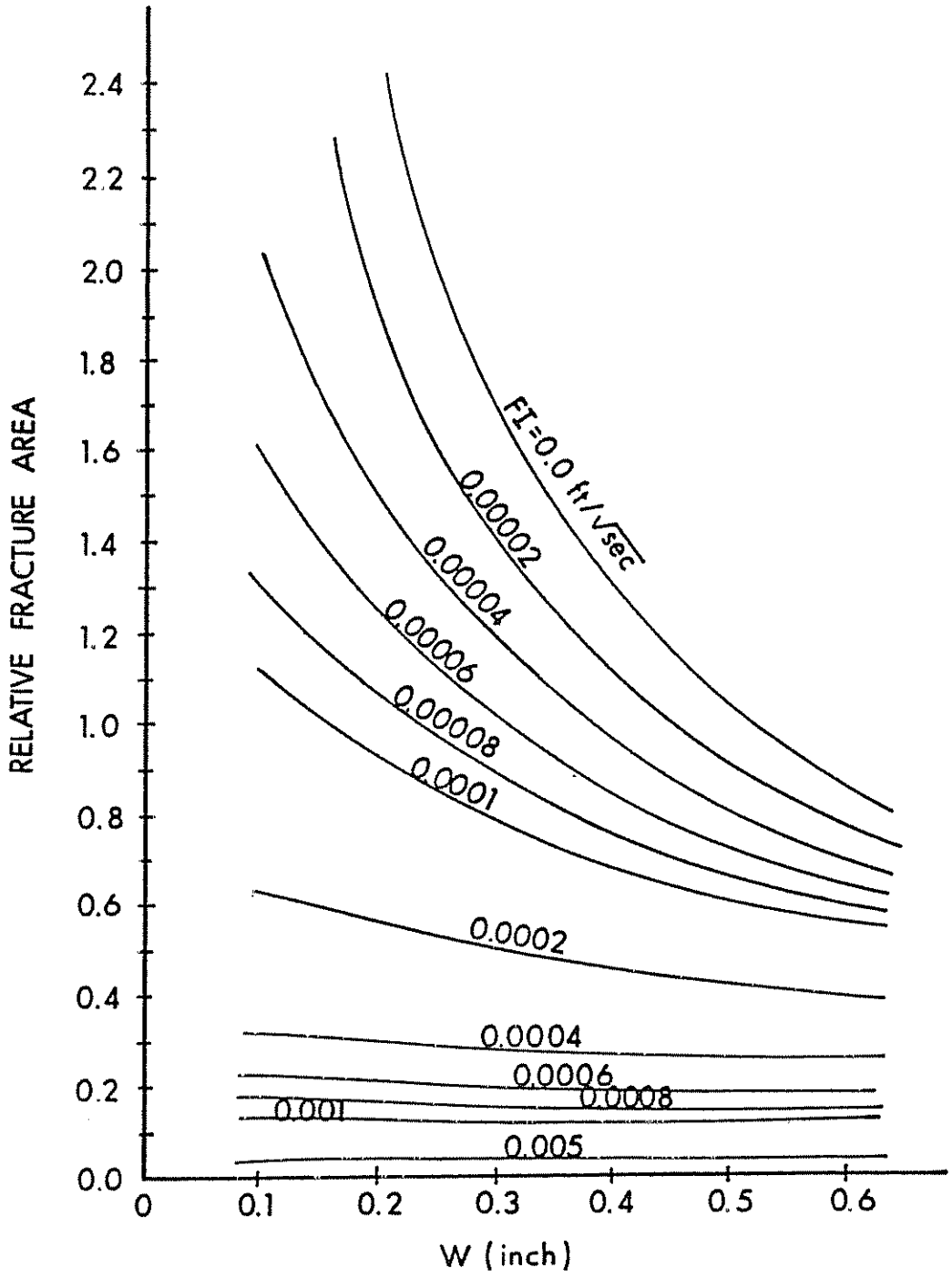

Figure 11: Fracture Area Scaling Curve for Different Fracture Widths.

from Figures 10 and 11. The leak-off ratio curves as a function of the flow index and fracture width are plotted in Figures 12 a, b, and c. Applicability of these curves along with the fracture width height predictive plots is illustrated in the section on applications.

The second type of fluid flow simulation is an extension of Nordgren's model [6] as presented by Geertsma and Haafkens [9]. The one dimensional fluid flow equation obtained from the mass conservation, momentum, and isotropic medium pressure-fracture width relations is

$$\frac{E}{128(1-\nu^2)2H\mu}\frac{\partial^2 W^2}{\partial x^2} - \frac{\partial W}{\partial t} = \frac{8C}{\pi(t-\tau(x))^{\frac{1}{2}}} \qquad (3)$$

$$0 \leq x \leq L,\ t \geq 0$$

where $\tau(x)$ is the elapsed time for the fracture to open at x. The initial condition $W(x,0) = 0$ is assumed along with the boundary conditions $W(x,t) = 0$ for $x \geq L(t)$ and the flow requirement

$$-\left(\frac{\partial W^4}{\partial x}\right)_{x=0} = \frac{256\mu(1-\nu^2)Q}{\pi E}$$

for a two sided fracture.

The steady state solution ($\partial W/\partial t = 0$) and finite difference results for the transient problem represented by equation (3) have been presented by Nordgren [6] and Geertsma and Haafkens [9]. The discretized finite element weak form of the extended version of the width equation, obtained by using the Geertsma procedure, is

$$K_{ij}(a)a^j(t) + C_{ij}\dot{a}^j(t) + F_i(t) = 0 \qquad (4)$$

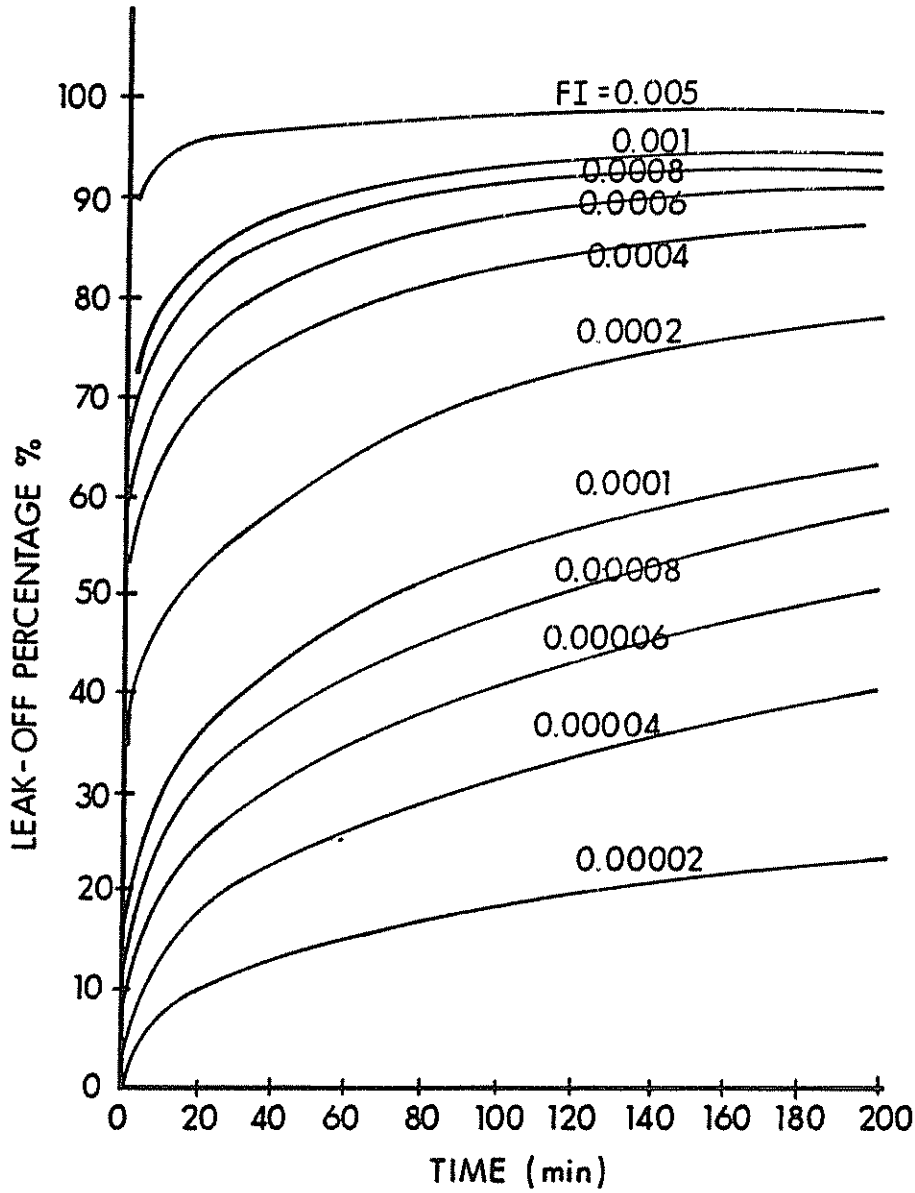

Figure 12a: Percentage Cumulative Fluid Leak-off Versus Treatment Time for Different Flow Indices (Width = 0.2 in).

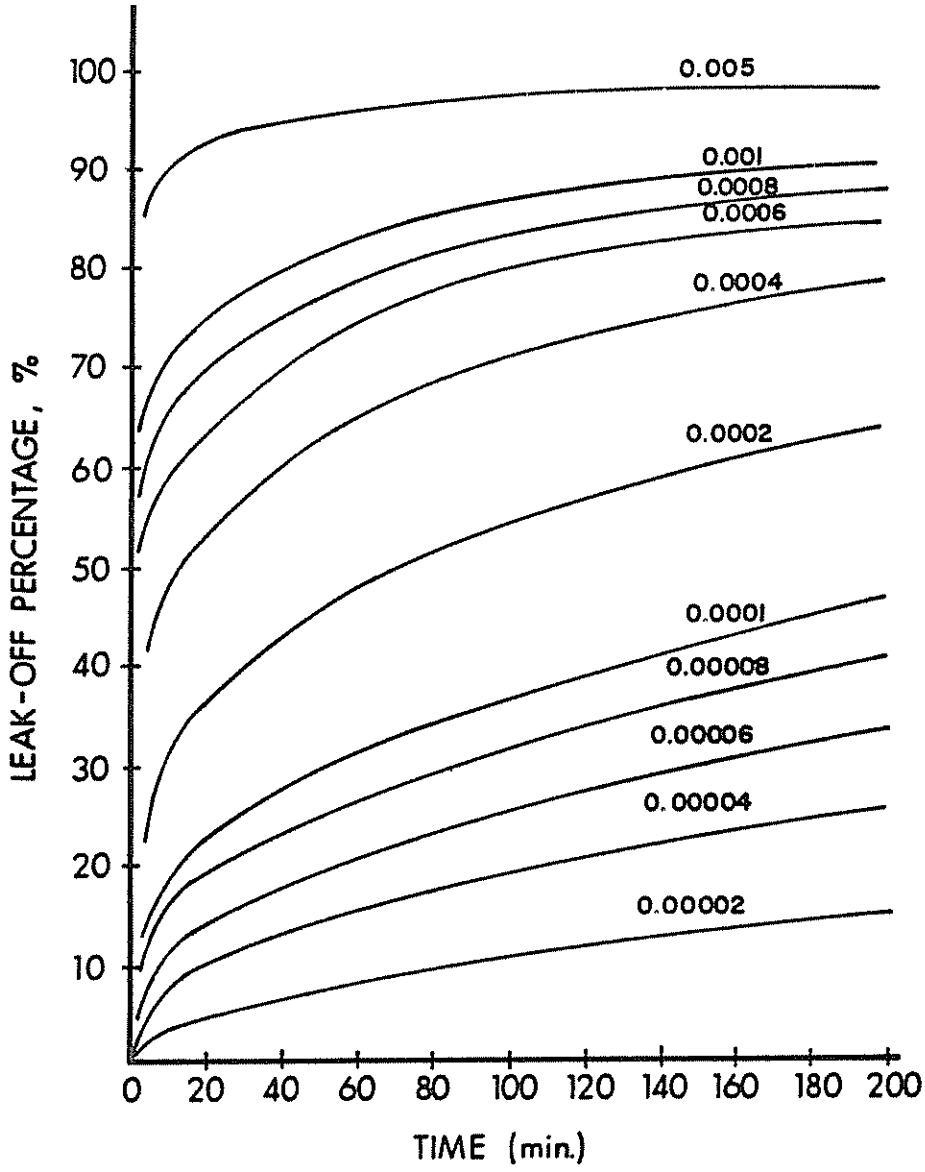

Figure 12b: Percentage Cumulative Fluid Leak-off Versus Treatment Time for Different Flow Indices (Width = 0.4 in).

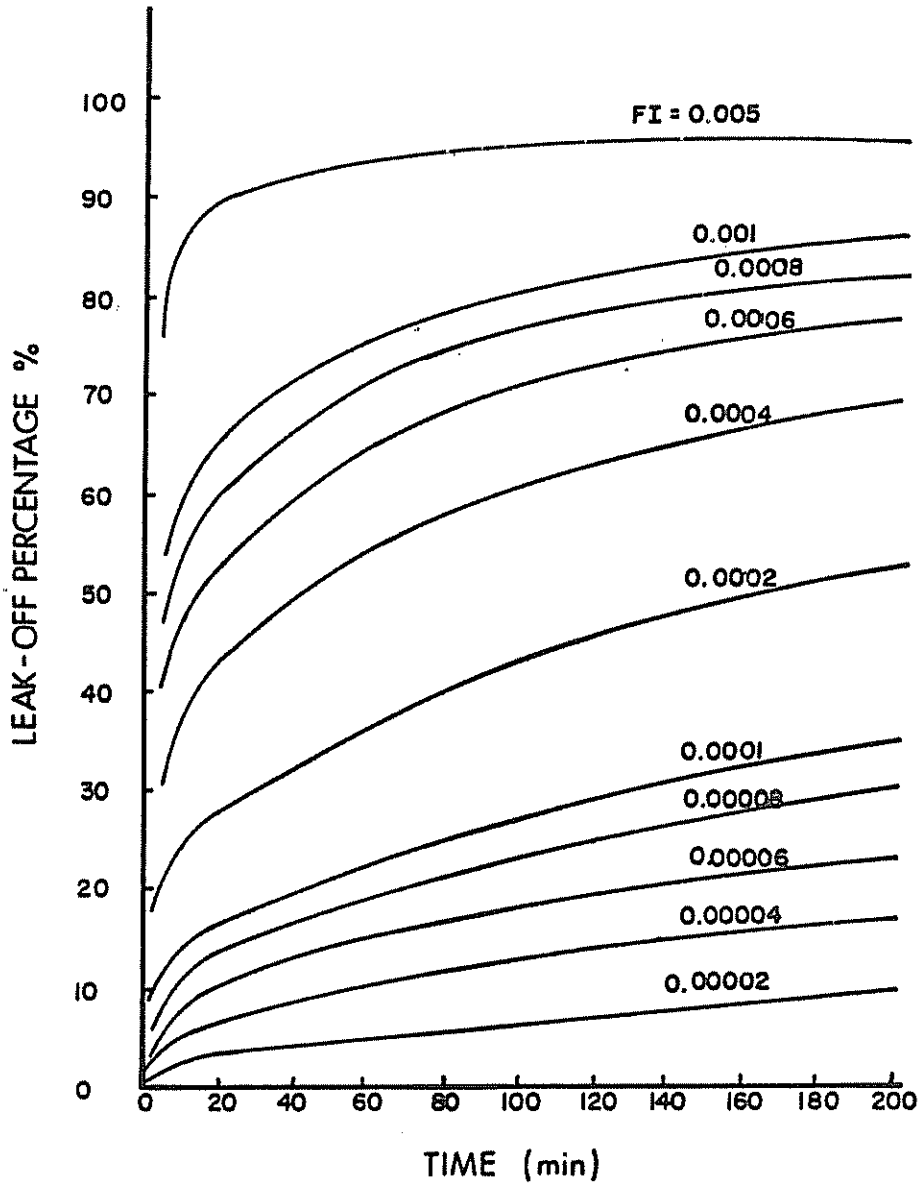

Figure 12c: Percentage Cumulative Fluid Leak-off Versus Treatment Time for Different Flow Indices (Width = 0.6 in).

where

$$K_{ij}(a) = \frac{E}{32(1-\nu^2)(2H)\mu}\int N_{i,x}^T (N_k a^k)^3 N_{j,x}\,dx$$

$$C_{ij} = \int N_i^T N_j\,dx$$

$$F_i(t) = \frac{8C}{\pi}\int \frac{N_i}{(t-\tau(x))^{\frac{1}{2}}}\,dx$$

where N_i is the selected interpolation function associated with the i-th node defined by

$$W(x,t) = N_i(x)a^i(t)$$

and commas designate differentiation

For the steady state problem, the appropriate version of Equation (4) is

$$K_{ij}a^j + F_i(t) = 0 \qquad (5)$$

with

$$K_{ij} = \frac{E}{128(1-\nu^2)2H\mu}\int N_{i,x}^T N_{j,x}\,dx$$

$$F_i = \frac{8C}{\pi}\int \frac{N_i}{(t-\tau(x))^{\frac{1}{2}}}\,dx$$

where N_i is defined by

$$W^4(x,t) = N_i(x)a^i(t)$$

Equation (5) is the familiar linear stiffness-force matrix formulation. On the other hand, the non-linearity inherent in the stiffness matrix for Equation (4) requires the solution of a non-linear set of algebraic equations. The isotropic medium steady state and transient width solutions can be extended to the multi-layered geometry case by use of the width scaling curves (Figures 6a, 6b).

For the steady state case, the width profile is obtained without difficulty for specified parameters. Figures 13a and 13b compare the computed steady state finite element width and pressure profiles with the "exact" Perkins and Kern [4] solution outlined by Geertsma and Haafkens [9]. The selected parameters are: Injection rate Q = 10BPM, injection time = 200 minutes, fracture height 2H = 100 ft., fluid loss coefficient C = 0.0015 ft/min$^{\frac{1}{2}}$, Poisson's ratio ν = 0.2, shear modulus G = E/2(1 + ν) = 2.6 x 10^6psi.

Discrete algorithms have been developed for the transient case with the non-linear system of Equation (4) considered at time intervals (t_n, t_{n+1}) [38]. The resulting non-linear algebraic equations are solved by the Newton-Raphson method. Figure 14 typically illustrates the transient width-length profiles as the fracture progresses. The fracture area and resulting length can then be computed from the finite element version of the mass balance equations with leak-off effects considered. For example, the "exact" solution with spurt losses neglected for the length (Carter's model) is [9]

$$L = \frac{Q\overline{W}}{16HC^2}\left[\frac{2\alpha}{\pi^{\frac{1}{2}}} - 1 + e^{\alpha^2}\ \mathrm{erfc}\ \alpha\right] \qquad (6)$$

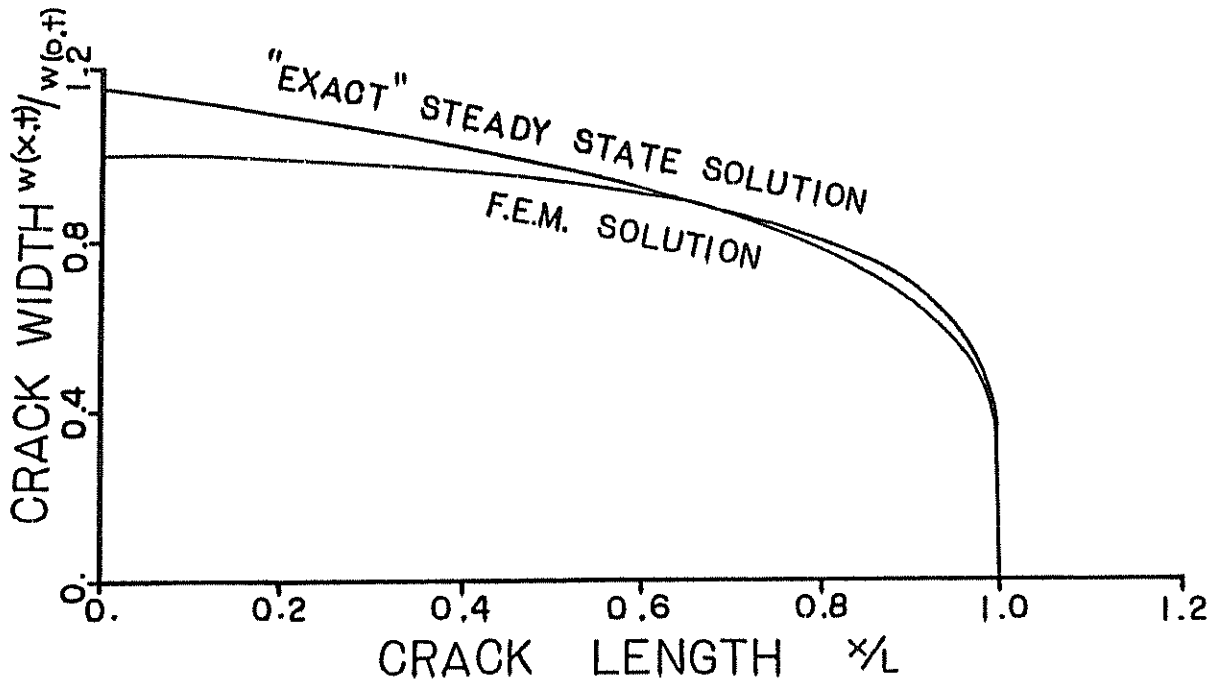

Figure 13a: Comparison of Finite Element Model Width Profile with Perkins and Kern [4] Analytical Solution.

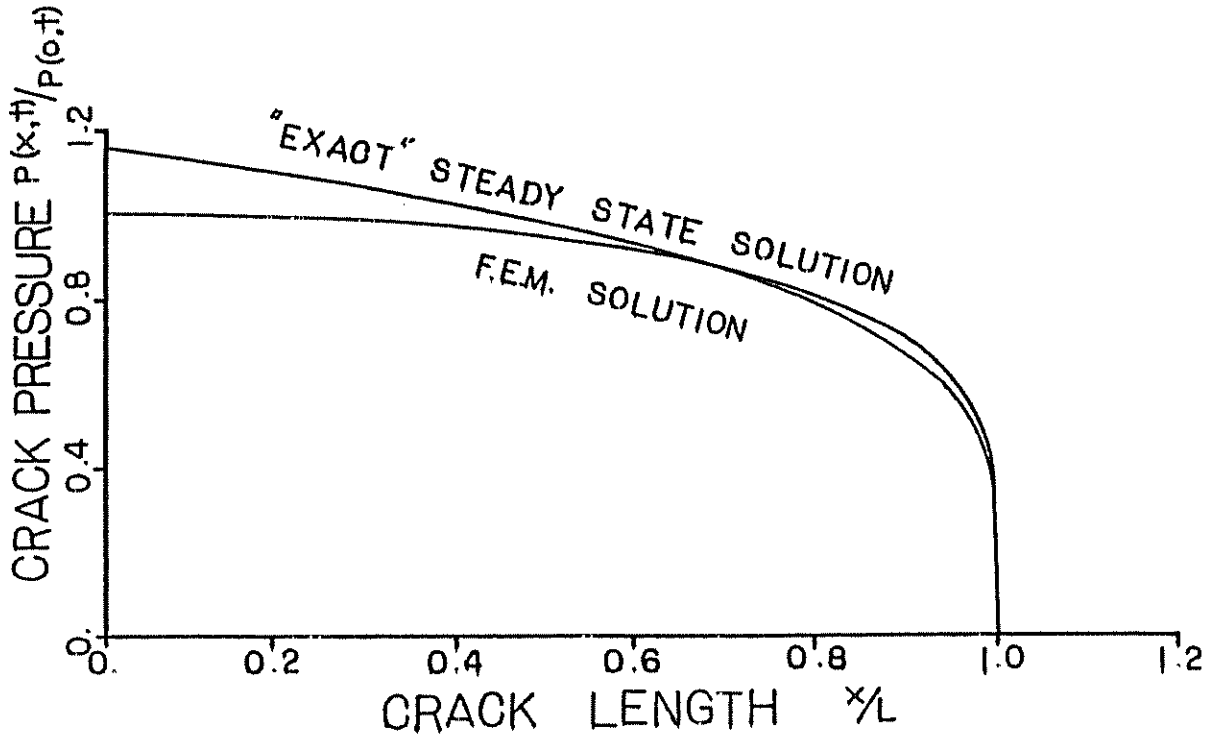

Figure 13b: Comparison of Finite Element Model Pressure Profile with Perkins and Kern [4] Analytical Solution.

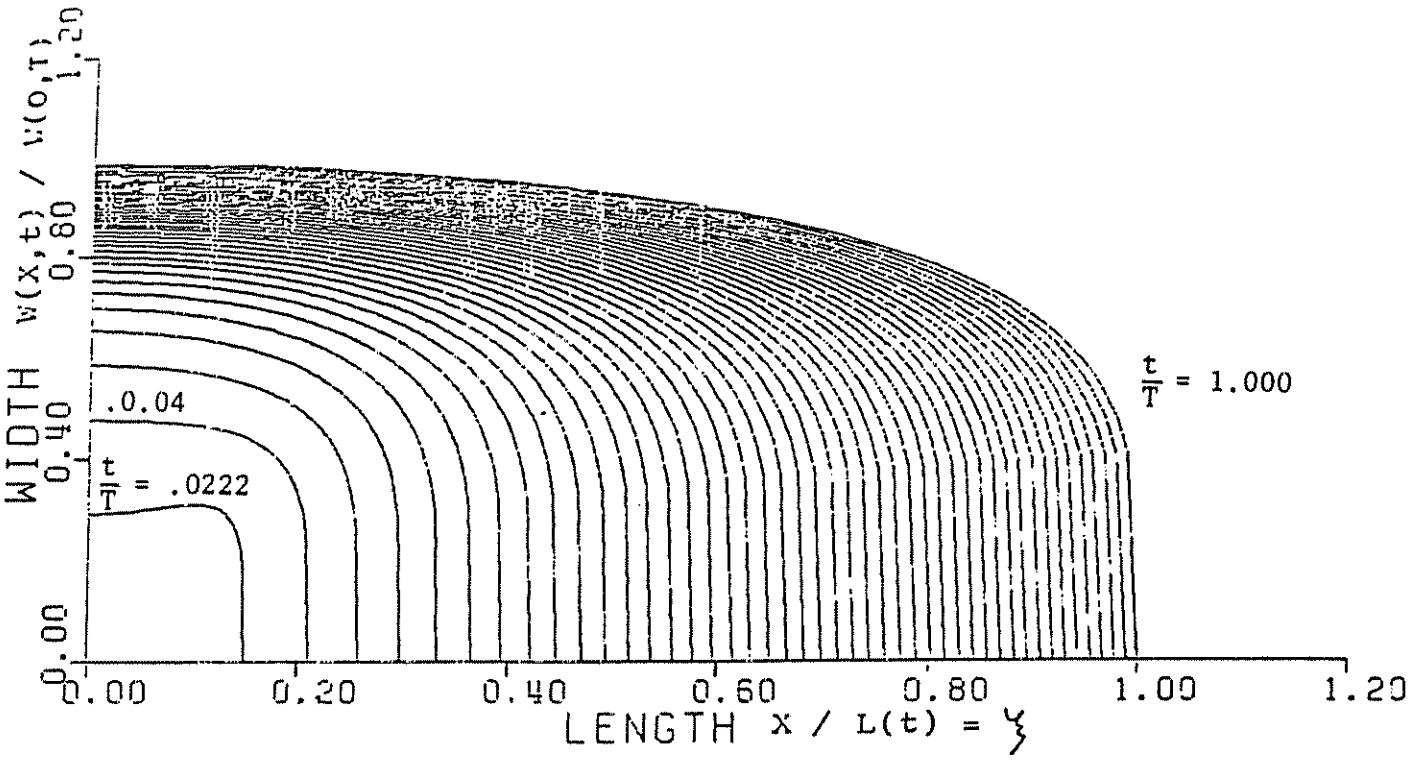

Figure 14: Transient Width Profile for a One-sided Fracture

where

$$\alpha = \frac{2C}{W} (\pi t)^{\frac{1}{2}}$$

Length comparisons employing the finite element solution, the finite difference formulation [37], and Equation (6) are in progress (Appendix A).

Modification of the preceding finite element analysis for the case of power law fracturing fluids ($\tau = \bar{\mu}\gamma^n$) can be accomplished by introducing the appropriate pressure gradient term in the momentum equation. The pressure gradient has the form

$$\frac{\partial}{\partial x} (\Delta p) = - C_1 \frac{\bar{\mu}}{W} \left[\left(\frac{2n' + 1}{n'} \right) \frac{Q}{2HW^2} \right]^{n'} \qquad (7)$$

where C_1 is a constant which depends on the vertical crack cross-section properties. Use of Equation (7) in lieu of the laminar Newtonian fluid relationship merely introduces a different exponent for the non-linear term in Equation (3). The corresponding width-flow rate equation for non-Newtonian fluids is given by Perkins and Kern [4].

Based on the above presentation, the finite element approach for the fluid flow simulations appears to be more general since it incorporates multi-layered media with differential tectonic stress as well as power law fluids.

3.3 Foam Fracture Simulations

The use of foam as a low residual fracturing fluid appears attractive for the low pressure, low temperature Devonian shale reservoirs. The efficiency and effective viscosity of foam generate large surface areas [38], [39]. The low liquid content is quickly returned to the surface by expansion of the nitrogen during flow back for well clean up. Laboratory tests using cores also indicate that foam is ideal as a fracturing fluid in terms of shale-fluid interaction and resulting formation swelling. The principal disadvantages of foam fracturing are the low amount of sand and its slow settling characteristics. In general, the use of 100 mesh sand is recommended for Devonian shale reservoirs to limit fluid leak-off. Foam has been widely used by industry over the last decade with good success in terms of well productivity [40], [41].

The foam displays Bingham plastic characteristics with the effective viscosity μ_e represented by

$$\mu_e = \mu_p + \alpha_1 \tau_y W^2 H/Q \qquad (8)$$

where μ_p is the plastic viscosity, α_1 is a constant, τ_y is the yield stress, W is the fracture width, H is the fracture height, and Q is the flow rate. This viscosity characterization can also be defined in terms of an equivalent shear stress-strain rate power law relationship and an averaged foam viscosity in the vertical crack can be assumed. The compressibility c of the foam, for a given foam quality and bottom hole treatment pressure, is employed for the evaluation of the bottom hole injection volume. Wide variations in the flow index or fluid loss coefficient for foam fracturing have been reported in the literature. This value apparently is in the range

from 10^{-5} ft/sec$^{-1/2}$[38] to 10^{-2} ft/sec^{-1} [42]. Based on an effective viscosity of 25 centipoise, obtained on 0.80 quality foam, from equation (8), permeability K = 0.1 m d, porosity = 5%, fluid pressure P_{BHTP} = 2000 psi, the computed loss coefficient is F I = 0.000086 ft/sec$^{1/2}$

The determined flow index FI can now be used to predict fracture dimensions for field experiments. As an example, for the zone 2 experiments on well # 20402 in Lincoln County, West Virginia [43], the target zone is the 250 ft thick dark brown shale bounded by the lighter gray shales. The stress gradient for this zone (σ_{HMIN} /$\sigma_{OVERBURDEN}$) is approximately 0.51. The estimated minimum horizontal in situ stress difference between the gray and brown shales of 800 psi and E_2/E_1 = 1.25 with an effective pressure of 300 psi (P_{BHTP} - σ_{HMIN}) yields a fracture height of 380 ft from the stress intensity versus height curves using the experimentally determined fracture toughness values for the two layers.

A surface injection rate of 40BPM for 180 minutes yields a fracture width of 0.33 in and corresponding fracture area of 0.748 x 10^6 ft^2.

3.4 Dendritic Fracture and Mixed Mode Fracture Simulations

The primary novelty associated with dendritic fracturing [44] is the procedure of stopping the injection of the fracture fluid and subsequently relieving the fluid pressure by allowing the fluid to flow back. The claims associated with this technique are that more fractures are created, that there is a larger tendency for branching fracture, and that spalling is induced which tends to prop the fracture so as to aid the flow of reservoir fluids during production. The use of the sand in the right amount, mesh size and sequence is indicated as a crucial factor in maximizing secondary fracturing. With coarse sand followed by the finer sand, it is possible to isolate the

primary crack and initiate secondary crack growth by modifying the pressure profile.

Secondary fracture propagation appears to depend largely on the difference in magnitude between the principal horizontal in situ stresses. The success of dendritic fracturing for certain reservoirs provides some clues regarding process mechanisms and desired reservoir properties. For example, the back flow has two beneficial features The first feature is the creation of fracture face spalling while the second effect is the change of the flow properties of the fracture when the accumulating sand and spalls have resulted in a significant increase in flow resistance. It seems that permitting the frac fluid to flow back momentarily after the primary fracture has been isolated may have a significant effect on the pressure distribution throughout the fracture system upon repressurization. The suggested mechanism can be illustrated by an analogy. It is believed that the fracture which continually accumulates sand due to the leak off of the frac fluid into the formation is similar to a filtering system. In a filtering system, as additional particles are filtered from the fluid, it becomes increasingly difficult for the fluid to penetrate. The increase in resistance to flow is accompanied by a steeper pressure gradient. While this is favorable for primary crack tip isolation, the pressure decrease can have a detrimental effect on secondary fracture propagation. Back flow of the frac fluid is analogous to back flushing the filtering system and should significantly reduce the resistance to flow in all parts of the fracture in which there was any significant reverse direction flow. It is noteworthy, because of the relatively short back flow durations, that the primary crack tip region will not be effectively back flushed and therefore

will essentially remain isolated from the pressure upon repressurization.

The spalling zone can be estimated from the solution to the one dimensional diffusion equation and use of the rock tensile fracture strength (S_t) and pore pressure (P_o) magnitudes. The resulting conditions for estimating spalling depth y are:

$$\frac{P_{BHTP} - S_t - \sigma_{HMIN}}{P_{BHTP} - P_o} = \text{erf } \xi \qquad (9)$$

for uniform propping and

$$\frac{P_{BHTP} - S_t}{P_{BHTP} - P_o} = \text{erf } \xi \qquad (10)$$

for non-uniform propping

where $\xi = y/2\ (K\ t/\mu\ \phi\ c)1/2$

Figures 15a and 15b typically illustrate the propped and unpropped spalling depth, respectively for different elapsed fracture treatment time durations.

Figure 16 illustrates the selected dendritic fracture model with a primary fracture and secondary crack subjected to pressure and in situ loading. Stress intensity factor plots, (Figures 18) using the configuration in Figure 17, have been obtained using both the energy release rate and J integral approaches. The values are plotted with the superposed results for selected values of σ_{HMIN}, σ_{HMAX}, and p illustrated in Figures 19a, b, c along with plots of $K^b_{effective}$ based on the energy release rate equation. The final combination of the horizontal stresses and crack pressure in Figures 19b, c illustrate the increased tendency for secondary crack propagation when the horizontal in situ principal stress magnitudes are

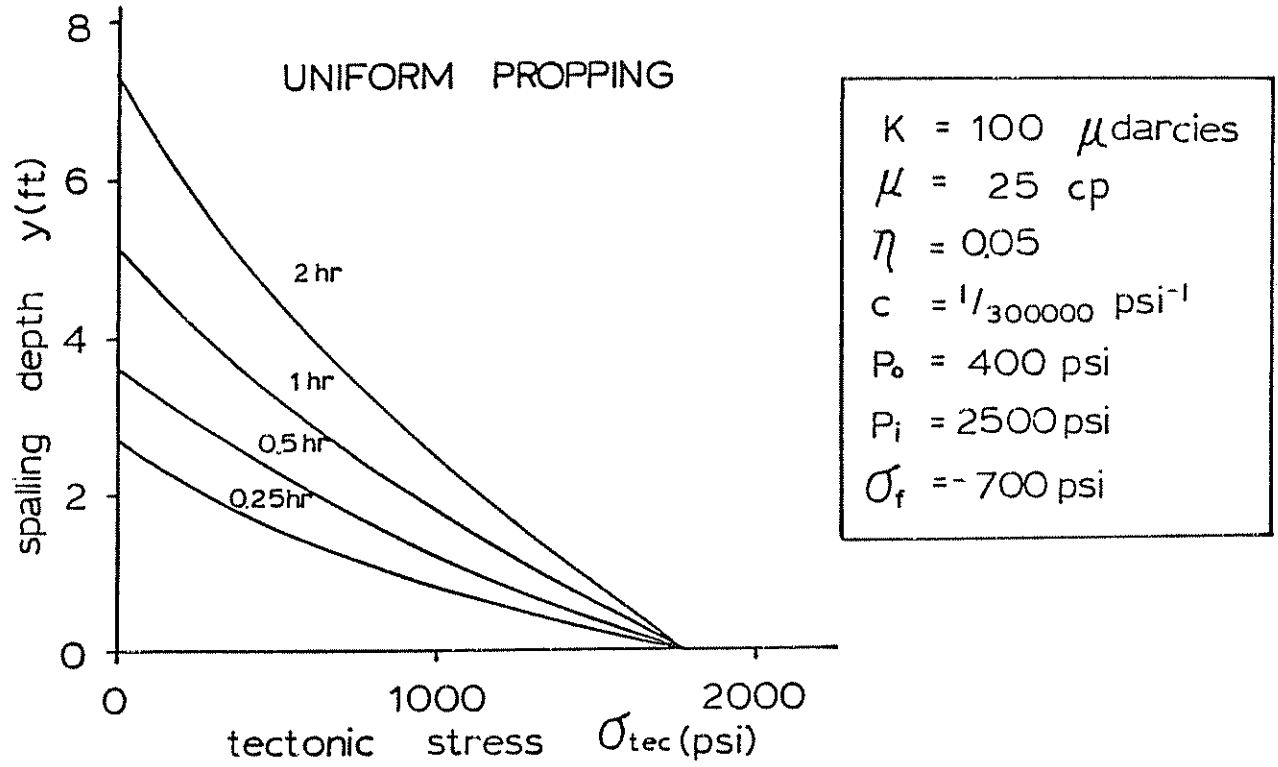

Figure 15a: Uniformly Propped Spalling Depth Versus Tectonic Stress for Different Time Durations.

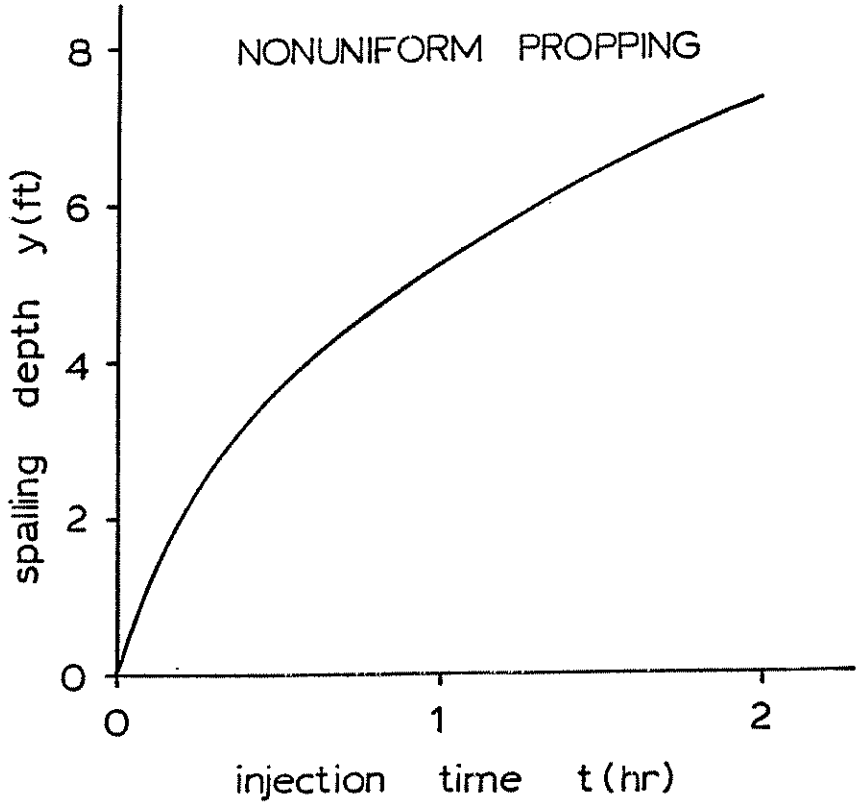

Figure 15b: Non-uniform Propping Versus Injection Time.

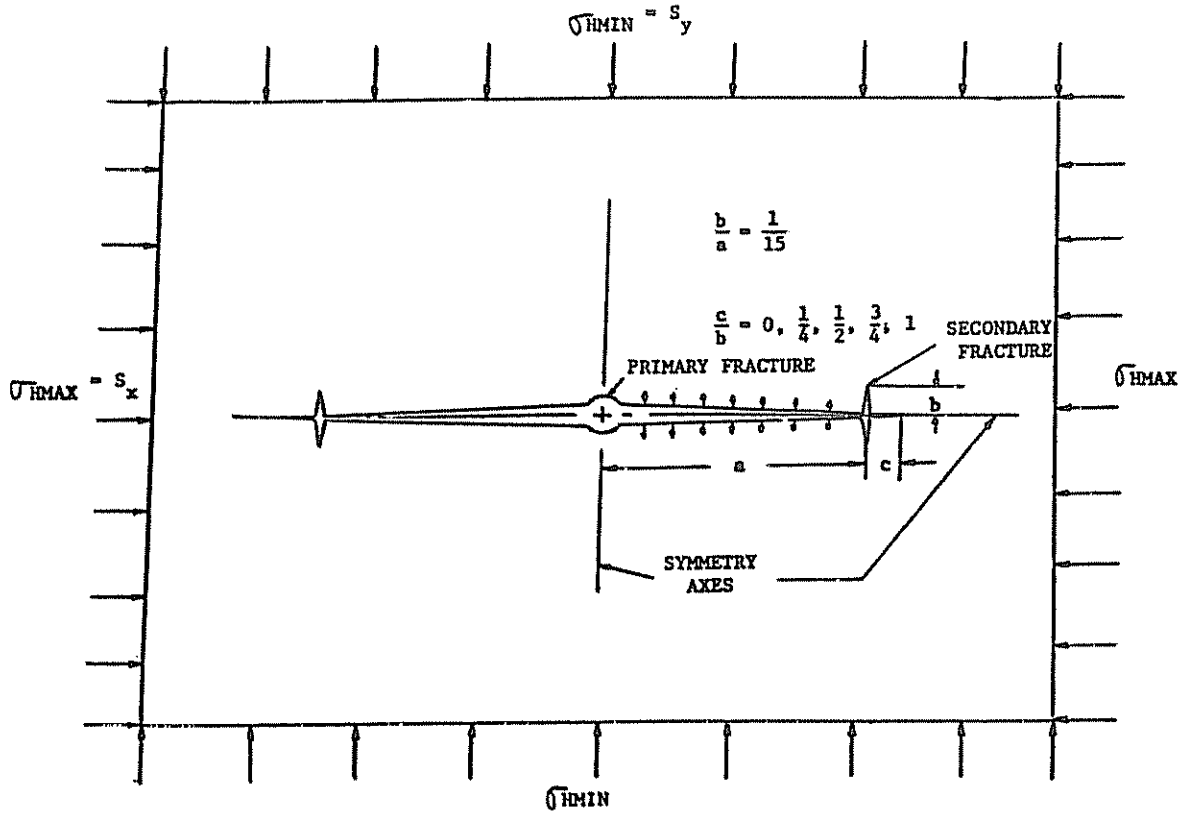

Figure 16: Dendritic Fracture Model with Primary and Secondary Fractures Subjected to In Situ and Pressure Loadings.

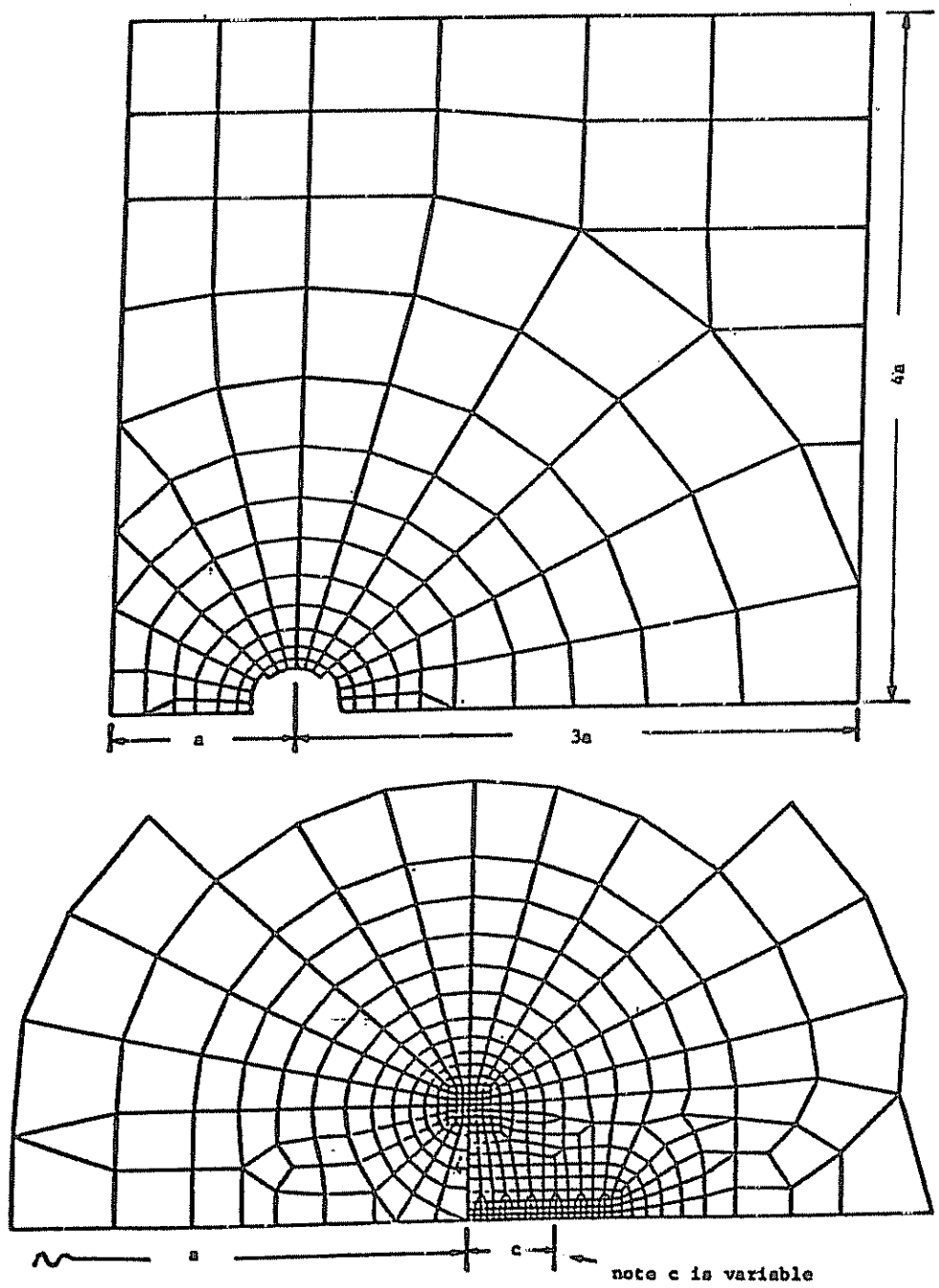

Figure 17: Selected Finite Element Configuration Corresponding to Dendritic Fracture Model. Lower Figure Provides Detail of Crack Tip Elements for Cut Out Section of Upper Figure.

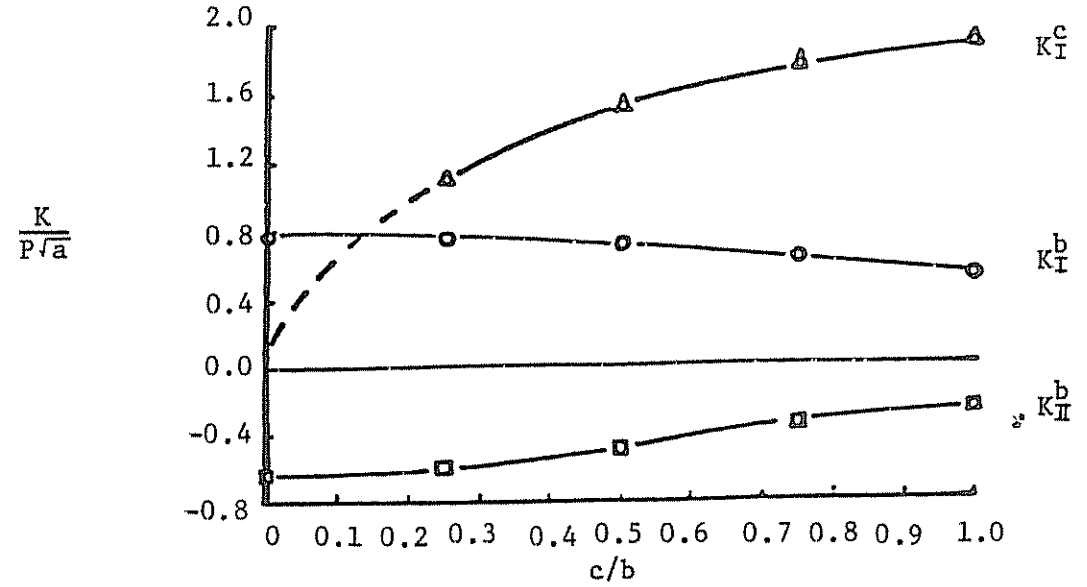

a. Pressure Applied to Fracture Faces

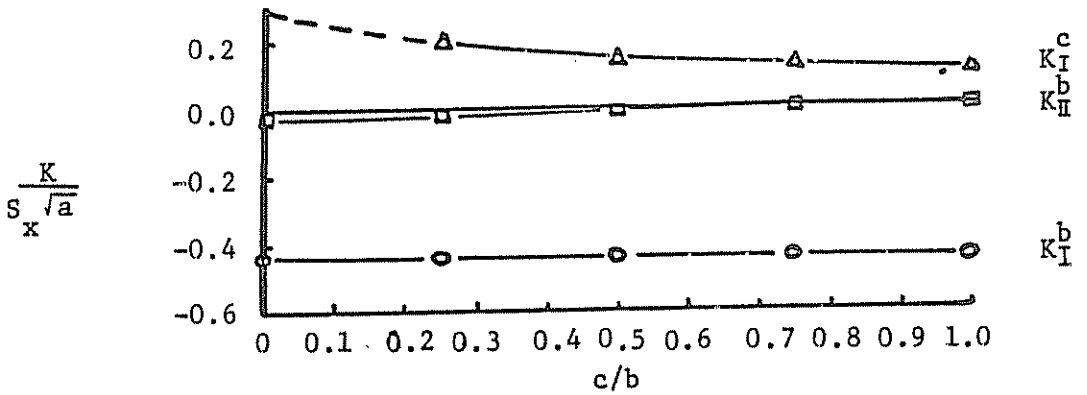

b. Remote X - Direction Stress

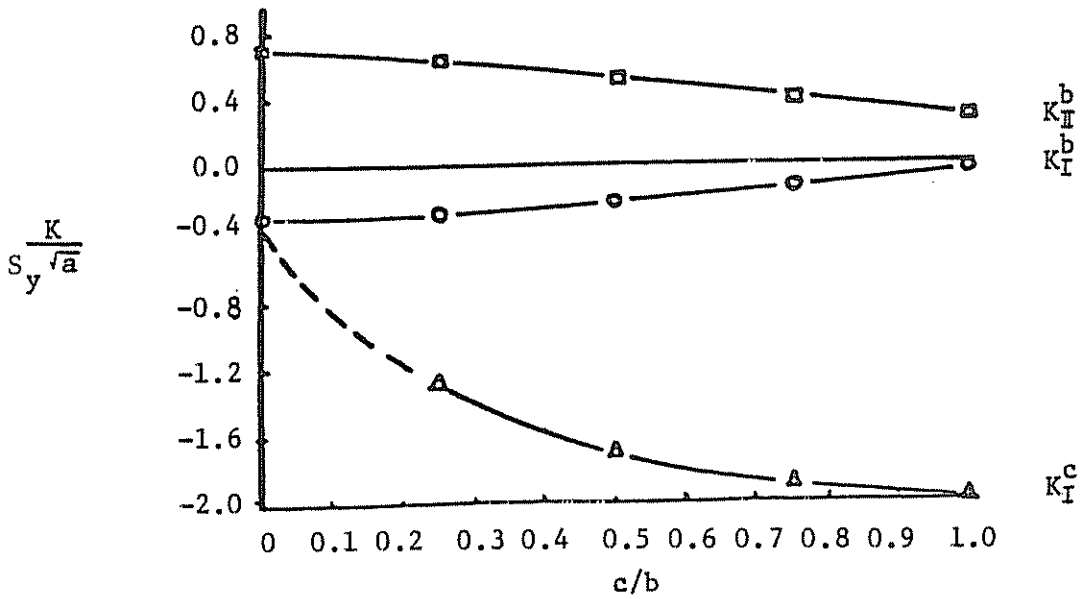

c. Remote Y - Direction Stress

Figure 18: Computed Stress Intensity Factors for Pressure and Horizontal In Situ Stress Loadings.

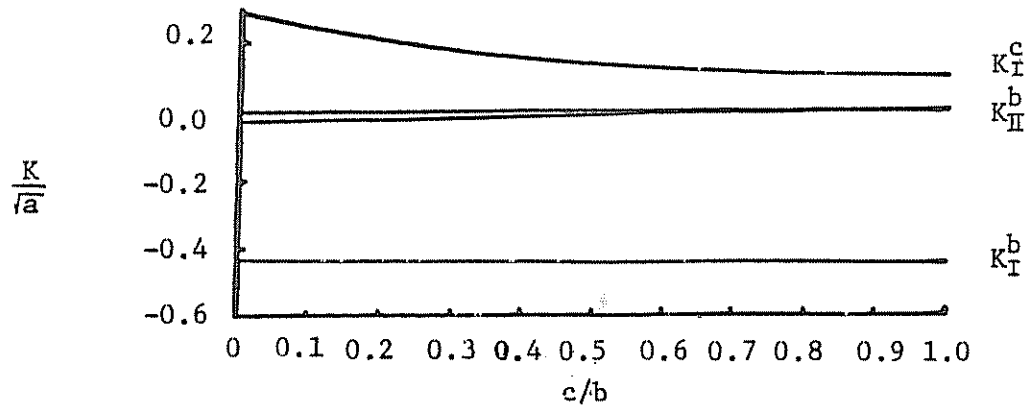

a. $P = S_y = 1$; $S_x = 2$

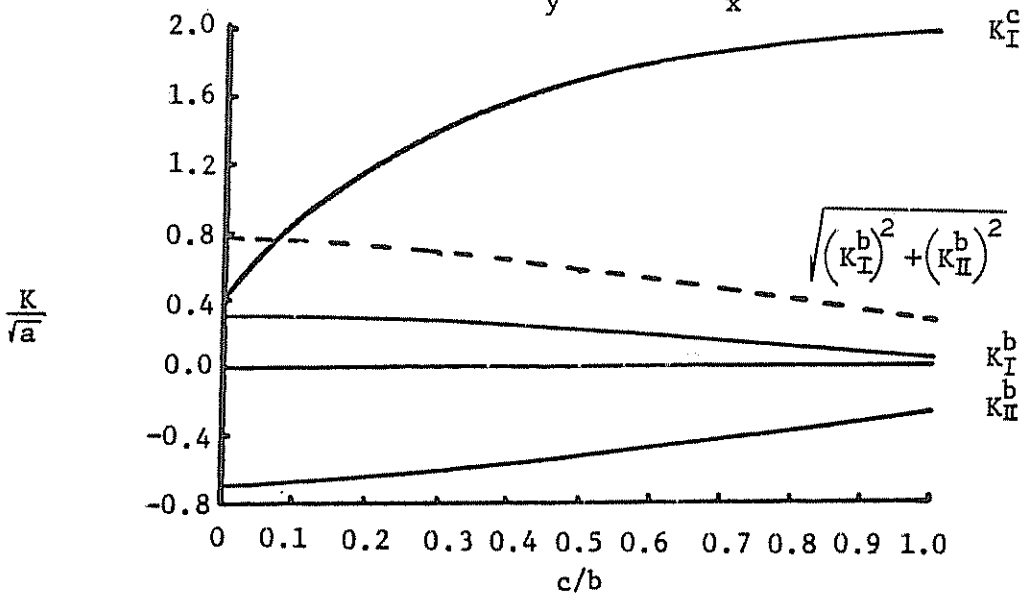

b. $P = S_x = 2$; $S_y = 1$

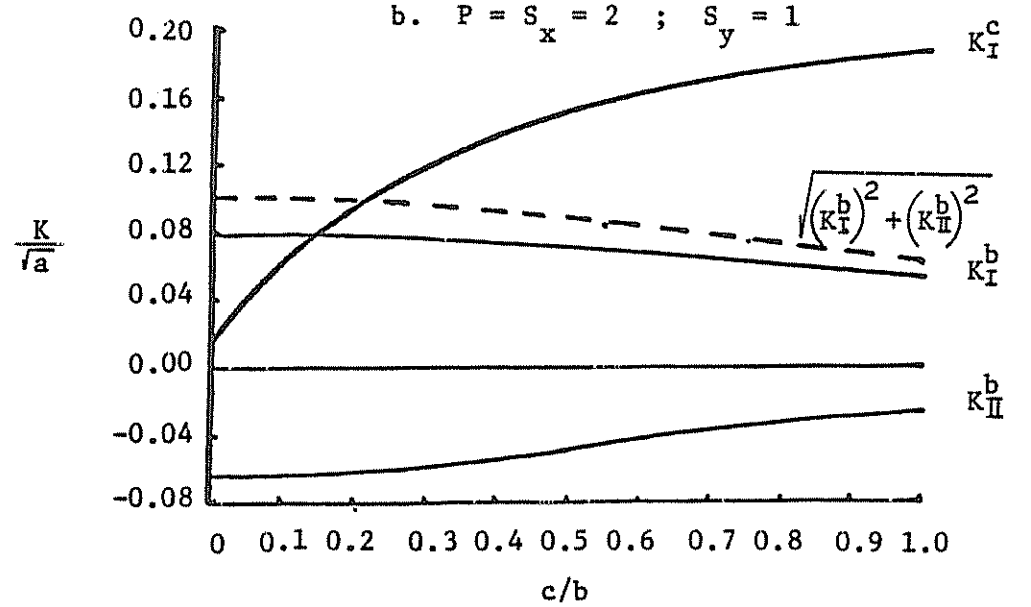

c. $S_x = S_y = 1$; $P = 1.1$

Figure 19: Computed Stress Intensity Factors for Combinations of Pressure and Horizontal In Situ Stress Loadings

relatively close. Branch cracking is revealed in Figures 19b and 19c for selected values of c/b. For example, in Figure 19c, K_I^b exceeds K_I^c for $0 < c/b \leq 0.255$. Stress contours resulting from the frac fluid pressure loading are typically illustrated in Figures 20a and 20b.

Another example of mixed mode conditions results from the interaction of the induced vertical fracture with a joint. Figure 21 illustrates a vertical crack interacting with a horizontal joint at a bi-material interface. The shear interaction at the joint interface coupled with the interactions of frac fluid pressure and in situ stresses can produce conditions favorable to crack propagation at the joint tip. For the case of a joint subjected solely to a uniform shear stress τ, the computed values of $K_I/\tau\sqrt{a}$ and $K_{II}/\tau\sqrt{a}$ at the joint tip one -0.198 and 0.593. These values when superposed with the in situ and frac fluid pressure stress intensity response can induce joint tip fracture propagation under mixed mode conditions.

Several mixed mode fracture intraction criteria are available in the literature. Ingraffea [45] has presented a comparison of the maximum hoop stress [46], minimum strain energy density [47], and maximum energy release rate [48] theories. In addition, a fracture criterion for rock media with the effects of crack closure and frictional effects has been recently developed by Advani and Lee [49]. These criteria are reviewed below:

(i) Crack Closure and Frictional Effects Theory

This theory, based on the maximum circumferential stress, includes the effects of crack closure and frictional effects. The failure threshold is defined by

$$\left(\frac{K_{II}}{2K_{IC}}\right)^2 + \left(\frac{K_I}{K_{IC}}\right) = 1 \qquad (11)$$

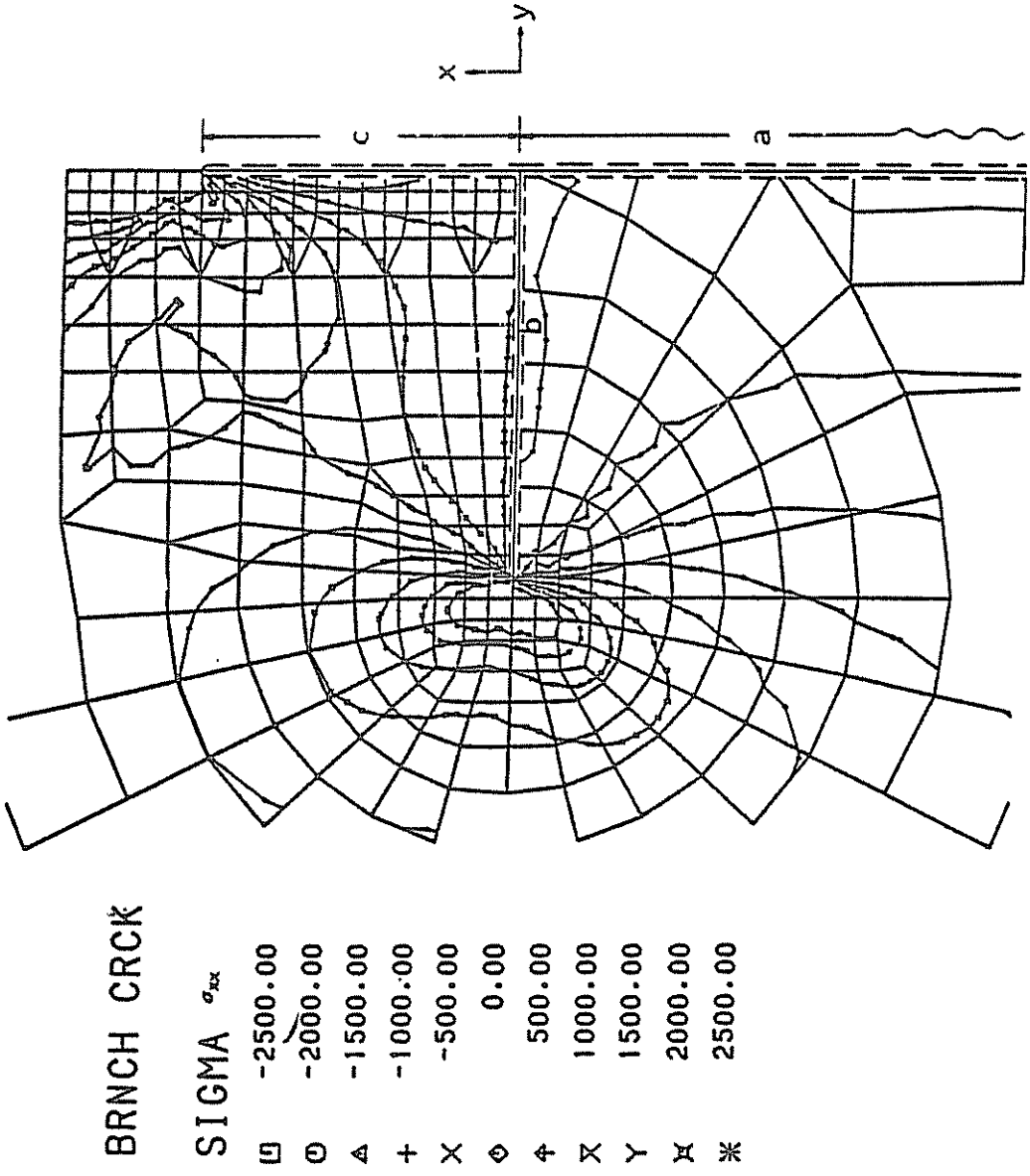

Figure 20a: Stress Contains σ_{xx} Induced by Frac Fluid Pressure Loading $\Delta p = 1000$ psi.

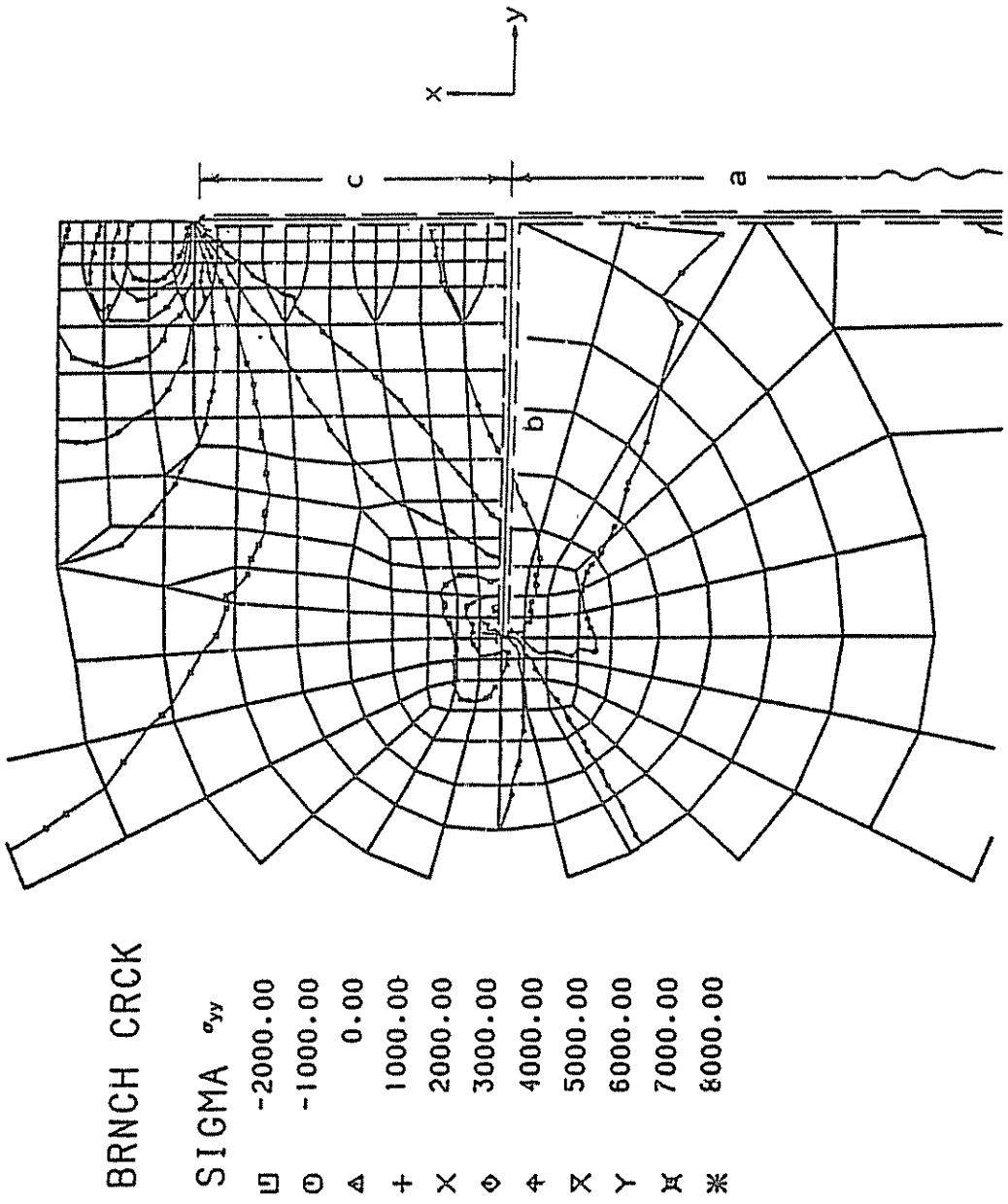

Figure 20b: Stress Contours σ_{yy} Induced by Frac Fluid Pressure Loading $\Delta p = 1000$ psi.

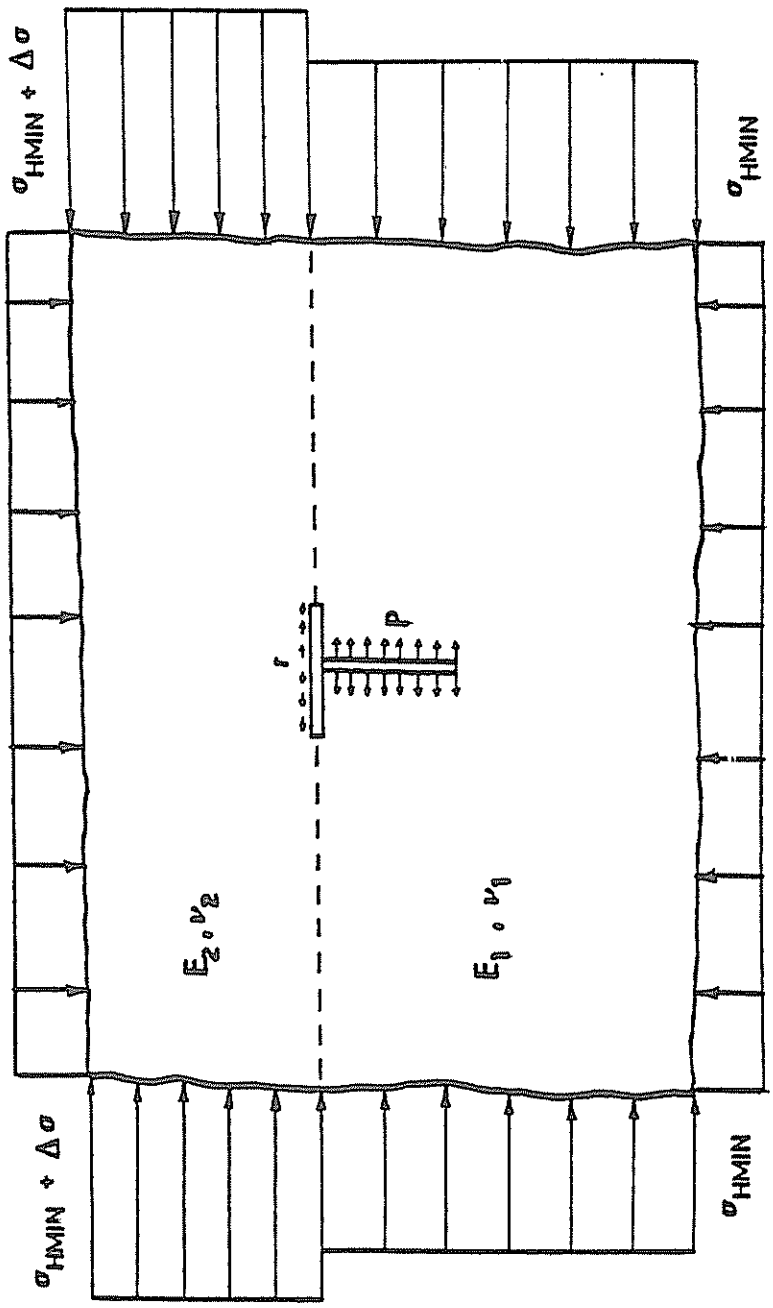

Figure 21: Joint-Vertical Crack Interaction Model with $E_2/E_1 = 1.25$.

(ii) Maximum Tensile Hoop Stress Theory

In this theory, the fracture envelope is defined by

$$\cos\frac{\theta}{2}\left[\frac{K_I}{K_{IC}}\cos^2\theta - \frac{3}{2}\frac{K_{II}}{K_{IC}}\sin\theta\right] = 1 \qquad (12a)$$

where the fracture angle θ is governed by

$$K_I \sin\theta + K_{II}(3\cos\theta - 1) = 0 \qquad (12b)$$

(iii) Maximum Strain Energy Release Rate

The fracture locus for this theory is defined by

$$\left(\frac{K_I}{K_{IC}}\right)^4 + 6\left(\frac{K_I}{K_{IC}}\right)\left(\frac{K_{II}}{K_{IC}}\right)^2 + \left(\frac{K_{II}}{K_{IC}}\right)^4 = 1 \qquad (13)$$

(iv) Minimum Strain Energy Density Theory

Fracture initiation for this theory is governed by

$$K_I^2(3 - 4\nu - \cos\theta)(1 + \cos\theta) + 4K_I K_{II}\sin\theta(\cos\theta - 1 + 2\nu) \qquad (14a)$$

$$+ K_{II}^2\, 4(1 - \nu)(1 - \cos\theta) + (1 + \cos\theta)(3\cos\theta - 1) = 4(1 - 2\nu)K_{IC}^2$$

with θ defined by

$$K_I^2(1 + \cos\theta)(2\cos\theta + 4\nu - 2) + 4K_I K_{II}(\cos\theta - (1 - 2\nu)\cos\theta)\sin\theta$$

$$+ K_{II}^2(2 - 4\nu - 6\cos\theta)\sin\theta = 0 \qquad (14b)$$

and the condition for stable crack propagation.

Figure 22 reveals the variation between the theories defined by the above equations. The selection of a specific theory, say for Devonian Shale or Pittsburgh coal, requires controlled mixed mode experiments. Its subsequent application to dendritic fracturing or joint interaction provides rationale and guidelines for field experiments.

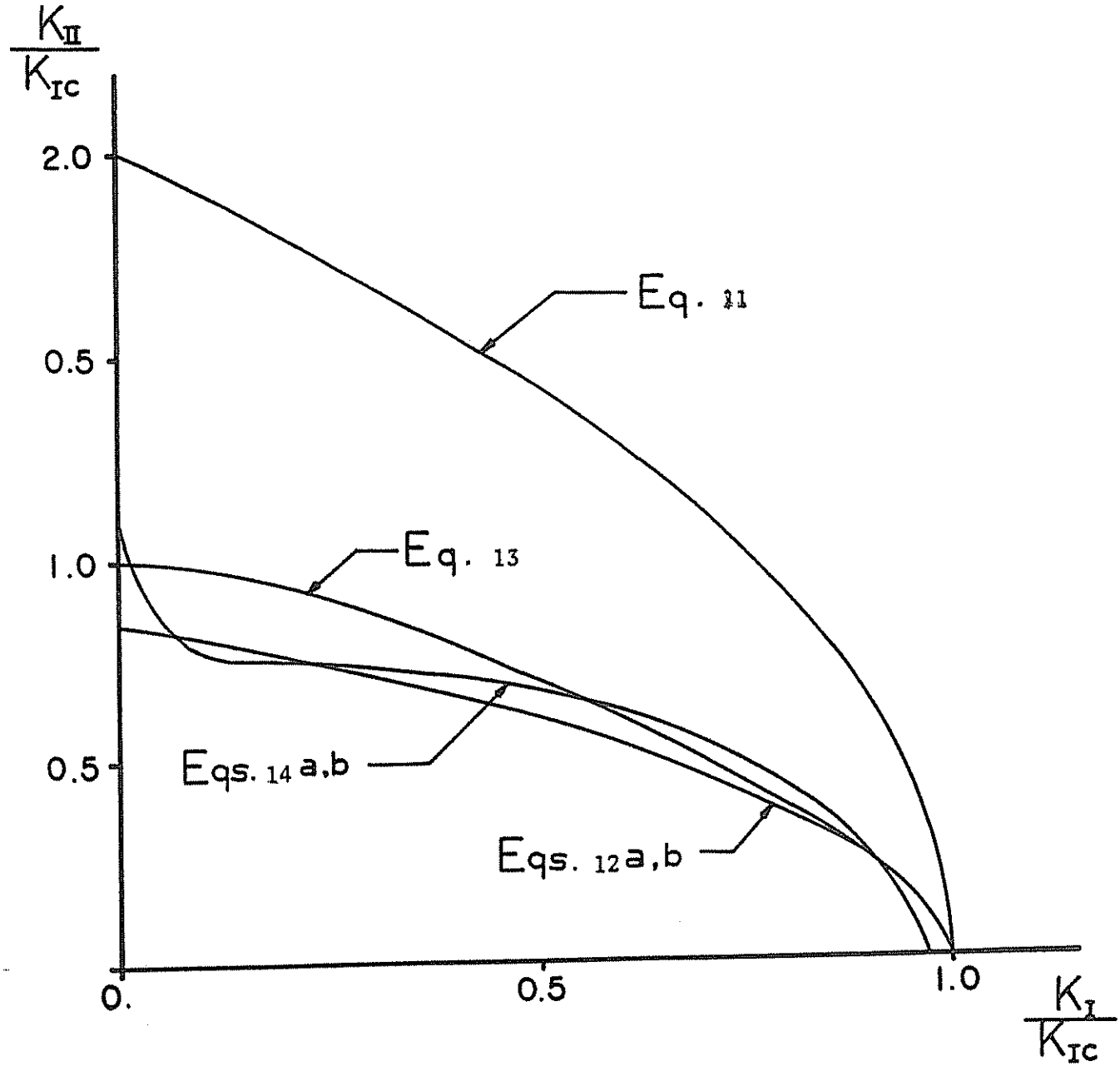

Figure 22: Comparison of Mixed Model Fracture Envelopes Using Different Theories.

4.0 APPLICATIONS AND EXAMPLES

In this section, the applicability of the model formulations and results reported in Section 3 is presented along with illustrative examples. A comparison of the available theories for predicting the vertical fracture widths and lengths is initially given using an example from Reference [9]. Analysis pertinent to the EGSP hydraulics fracturing field experiments is then provided. In addition, the role of in situ stresses and associated computations are discussed from the vantage point of stimulation design.

4.1 Comparison of Fracture Widths and Lengths for Various Theories

Prior to the specific application of the developed hydraulic fracturing code to field experiments for the EGSP, results from a sample problem illustrating the predicted fracture widths and extents using various theories are presented for bench mark comparison. The selected treatment and reservoir parameters are as follows [9]:

Fluid pumped volume = 600 bbls; Flow rate = 10 bbl/min;

Fluid loss coefficient = 0.0015 $ft/min^{1/2}$ (0.0001938 $ft/sec^{1/2}$);

Fracture height = 100 ft; Poisson's ratio = 0.15;

Shear modulus = 2.6 X 10^6 psi.

Table I reveals the predicted fracture lengths and widths for the different theoretical formulations:

Table I
Predicted Fracture Lengths and Widths

	Geertsma & DeKlark	Daneshy	Perkins & Kern	Nordgren	Advani et al*
Fracture Length	395 ft	360 ft	410 ft	485 ft	495 ft
Fracture Width	0.15 in	0.20 in	0.16 in	0.14 in	0.19 in

4.2 Illustrative Examples for the EGSP

Examples illustrating the prediction of fracture geometry from field experiments are presented here. Additional results are provided in Appendix C. Field data for three shale foam fracturing experiments is provided in Table II.

* Spurt loss effects ignored and fluid flow program detailed in Reference [37] employed in the analysis.

Table II

Field Data for Hydraulic Fracture Experiments

Well No.	Permeability mD	Porosity %	Viscosity cp	P_{break}† psi	P_{ext}†	$P_{shut\ in}$† psi	Flow Rate BPM	Treatment minutes	Pore Pressure psi
Columbia #20403-1	0.1	5	46	2687	2367	1637	9.3	150	612
Columbia #20403-2	0.1	5	46	2096	1996	1246	9.4	168	555
Welch #1-15	0.1	5	46	2034	1824	1024	6.4	46	300

† Adjusted for bottom hole treatment conditions

The computed in situ stresses and rectangular fracture geometry predictions based on assumed formation material properties are given in Table III.

Table III

In Situ Stress and Fracture Geometry Predictions

Well No.	σ_{HMIN} psi	σ_{HMAX} psi	σ_{OVBD} psi	Average Width in	Fracture Height† ft	Fracture Length ft
Columbia #20403-1	1637	2611	3668	0.268	173	1260
Columbia #20403-2	1246	2087	3322	0.258	242	953
Welch #1-15	1024	1638	1463	0.218	72	925

† Fracture Height estimated from perforation and effective bottom hole pressure data.

The magnitudes of the stress gradients ($\sigma_{HMIN}/\sigma_{OVBD}$) and orientations of the horizontal principal stresses provide significant information relating to the fracture density and selection of the appropriate stimulation treatment. For example, the stress gradient magnitude of 0.45 for Columbia Gas well #20403-1 suggests a tectonically relaxed reservoir formation with a high systematic fracture density. A conventional foam fracture (low leak-off), cyrogenic or explosive fracture treatment appears to be suitable for this state of stress. On the other hand for stress gradients exceeding 0.55 and/or relatively "isotropic" stress fields, mini-massive scale gelled or dendritic treatments appear to be desirable. Specific recommendations will require correlations among stress magnitudes, treatment design variables, and production history for various sites.

5.0 CONCLUSIONS AND RECOMMENDATIONS

The presented frac fluid flow, structure, and fracture mechanics simulations provide an integrated basis for predicting and optimizing fracture dimensions and fluid leak-offs. The roles of in situ stress and material properties for possible vertical migration of fractures from the pay zone are discussed. Rationale for foam and dendritic fracturing experiments is presented along with numerical experiments for examining the phenomena of spalling of the fracture faces and conditions for secondary fracture initiation.

Several characteristics for the assignment of conventional, foam, cyrogenic, dendritic, and explosive fracturing treatments for specific reservoir properties have emerged. The controlling variables include consideration of the fracture density and extent, shale thickness, in situ stress gradients, energy assist mechanisms, well clean-up, shale-frac fluid interaction, proppant selection, and fracture height control. The analysis here suggests that correlation with prevailing in situ stress gradients are promising diagnostic indicators for fracture treatment selection and design. For example, for stress gradient magnitudes below 0.55, the higher natural fracture densities can be exploited in the treatment design. It is therefore desirable to study various basement-structure interaction phenomena and associated mechanisms responsible for in situ relief, natural fracture propagation, preferential fracture system orientations, and pore pressure effects.

In conclusion, the comprehensive development of an economical strategy requires extensive and controlled field testing with supporting

predictive analyses of reservoir responses. Finite element modeling of reservoir in situ stress trajectories based on the defined material, geometric, and structural properties is recommended. The flow and fracture responses in the reservoir can also be simultaneously modeled by use of finite element techniques.

6.0 REFERENCES

1. Howard, G.C. and C.R. Fast, "Hydraulic Fracturing," Society of Petroleum Engineers Monograph, Volume 2, 1970.

2. Anon., " The Fracbook Design/Data Manual for Hydraulic Fracturing," Halliburton Services, Duncan, Oklahoma, 1971.

3. Zheltov, Yu. P. and S.A. Kristianovitch, "The Hydraulic Fracturing of an Oil-Producing Formation," Isvest. Aked. Nauk SSSR, Otdel Tekh Nauk, No. 3, 41, 1955.

4. Perkins, T.K. and L.R. Kern, "Widths of Hydraulic Fractures," Journal of Petroleum Technology, 937, 1961.

5. Haimson, B. and C. Fairhurst, "Initiation and Extension of Hydraulic Fractures in Rocks," Society of Petroleum Engineers Journal, 7, 310, 1967.

6. Nordgren, R.P., "Propagation of a Vertical Hydraulic Fracture," Society of Petroleum Engineers Journal 253, 306, 1972.

7. Geertsma, J. and F. DeKlerk, "A Rapid Method of Predicting Width and Extent of Hydraulic Induced Fractures," Journal of Petroleum Technology, 1571, 1969.

8. Daneshy, A.A., "On the Design of Vertical Hydraulic Fractures," Journal of Petroleum Technology, 83, 1973.

9. Geertsma, J. and R. Haafkens, "A Comparison of the Theories for Predicting Width and Extent of Vertical Hydraulically Induced Fractures," Journal of Energy Resources Technology, ASME, 101, 8, 1979.

10. Advani, S.H. et al, "Analytical and Experimental Investigations on Induced Fracturing of Reservoir Rock," ASME Paper No. 76 - Pet 8, 1976.

11. Advani, S.H. et al, "Material and Structural Mechanics Simulations Associated with Hydraulic Fracturing Operations," Proceedings International Conference on Computer Simulation for Material Applications, Nuclear Metellurgy, Vol. 20, Part 2, pp. 1011-1022, 1976.

12. Shuck, L.Z. and S.H. Advani, "Induced Stresses in Hydraulic Fracturing Operations," Proceedings 15th Conference on Rock Mechanics, ASCE Publication, pp. 93-134, 1975.

13. Rice, J.R. and M.P. Cleary, "Some Basic Stress Diffusion Solutions for Fluid-Saturated Elastic Porous Media with Compressible Constituents," Reviews of Geophysics and Space Physics, 14, 227, 1976.

14. Ruina, A., "Influence of Coupled Deformation-Diffusion Effects on the Retardation of Hydraulic Fracture," Proceedings 19th U.S. Symposium on Rock Mechanics, 274, 1978.

15. Daneshy, A.A., "Hydraulic Fracture Propagation in Layered Formations," Society of Petroleum Engineers, Inc., Paper No. 6088, 1976.

16. Simonsen, E.R. et al, "Containment of Massive Hydraulic Fractures," Society of Petroleum Engineers, Inc., Paper No. 6089, 1976.

17. Advani, S.H. et al, "Hydraulic Fracture Modeling for the Eastern Gas Shales Projects," Proceedings Second Annual Eastern Gas Shales Symposium, METC/SP - 78/6, Vol. I, pp. 84-98, 1978.

18. Cleary, M.P., "Primary Factors Governing Hydraulic Fractures in Heterogeneous Stratified Porous Formations," ASME Paper No. 78-Pet - 47, 1978.

19. Hanson, M.E., "Theoretical and Experimental Research on Hydraulic Fracturing, Journal of Energy Resources Technology, ASME Transactions, 102, 92, 1980.

20. Advani, S.H. et al, "Rock Mechanics Aspects of Hydraulic Fracturing in the Devonian Shale," Proceedings 21st U.S. Symposium on Rock Mechanics, 1980, in Press.

21. Anon, "Vertical Hydraulic Fracture Design Code," TerraTek Report TR 78-56, 1978.

22. Hanson, M.E. et al, "Effects of Various Parameters on Hydraulic Fracture Geometry," Proceedings Unconventional Gas Recovery Symposium, Also Paper No. SPE/DOE 8942, 1980.

23. Mastrojannis, E.N. et al, "Growth of Planar Cracks Induced by Hydraulic fracturing," International Journal for Numerical Methods in Engineering, 15, 41, 1980.

24. Cremean, S.P. et al, "Novel Fracturing Treatments in the Devonian Shale," MERC/SP - 78/6, Vol. I, pp. 25-34, 1978.

25. McKetta, S.F. "Investigation of Hydraulic Fracturing Technology in the Devonian Shale," MERC/SP - 78, 6, Vol. I, pp. 25-34, 1978.

26. Marshall, R., Mitchell Energy, Personal Communications, 1980.

27. "Enhanced Gas Recovery Program," Northrop, D.A. and C.L. Schuster, Editors, Fourth Annual Report, October 1978 through September 1979, Sandia Laboratories Report SAND 79-2428, 1979.

28. Anderson, G.D., "The Effects of Mechanical and Frictional Rock Properties of Hydraulic Fracture Growth Near Unbounded Interfaces," Society of Petroleum Engineers, Inc., SPE 8347, 1979.

29. Holmes, B.S. and M.B. Rubin, "Proppant Fracture Mechanics Interaction Study of the Flow Fracture Process," SRI International Progress Reports, Contract No. AC-21-79 MC 11597, 1980.

30. Komar, C.A., "Development of a Rationale for Stimulation Design in the Shale," Society of Petroleum Engineers, Inc. SPE 7166, 1978.

31. Nolte, K.G. and M.B. Smith, "Interpretation of Fracturing Pressures," Society of Petroleum Engineers, Inc., SPE 8297, 1978.

32. Nolte, K.G., "Determination of Fracture Parameters from Fracturing Pressure Decline," Society of Petroleum Engineers, Inc., SPE 8 341, 1979.

33. Novotny, E.J., "Proppant Transport," Society of Petroleum Engineers, Inc., SPE 6813, 1977.

34. Daneshy, A.A., "Numerical Solution of Sand Transport in Hydraulic Fracturing, Journal of Petroleum Technology, 132, 1978.

35. Setari, A. and H. S. Price, "Simulation of Hydraulic Fracturing in Low Permeability Reservoirs," SPE/DOE 8939, 1980.

36. Advani, S.H., "Finite Element Model Simulations Associated with Hydraulic Fracturing," SPE/DOE 8941, 1980.

37. Chang, H-Y, "Development of Improved Design Criteria for Hydraulic Fracturing Operations," METC/CR - 78/11, 1978.

38. Hung, F.S., "Finite Element Model Simulations Associated with Hydraulic Fracturing," M.S. Thesis, The Ohio State University, 1980.

39. Blauer, R.E. and C.A. Kolhaas, "Formation Fracturing with Foam," Society of Petroleum Engineers Inc., SPE 5003, 1974.

40. Komar, C.A. et al, "Practical Aspects of Foam Fracturing in the Devonian Shale," Society of Petroleum Engineers Inc., SPE 8345, 1978.

41. Gaydos, J.S. and P.C. Harris, "Foam Fracturing: Theories, Procedures and Results, SPE/DOE 8961, 1980.

42. King, G.E., "Factors Affecting Dynamic Fluid Leak-off with Foam Fracturing," Society of Petroleum Engineers, Inc., SPE 6817, 1978.

43. Cremean, S.P. et al, "Massive Hydraulic Fracturing Experiments of the Devonian Shale in Lincoln County, West Virginia," Final Report, Columbia Gas/DOE Contract E(46-1) - 8014, January, 1979.

44. Kiel, O.M., "Hydraulic Fracturing Process Using Reverse Flow," U.S. Patent # 3,933,205, 1976.

APPENDIX A

FINITE ELEMENT SOLUTION OF LENGTH FROM ONE DIMENSIONAL INTEGRO-DIFFERENTIAL EQUATION

Equation (6) represents the one dimensional solution to the integro-differential equation of the Volterra type, namely

$$\frac{3\pi}{8} W \frac{dL}{dt} + 2C \int_0^t \frac{dL}{d\tau} \frac{d\tau}{(t-\tau)1/2} = \frac{Q}{H} \tag{A-1}$$

with the boundary condition $L(0) = 0$

The above equation has the standard form

$$\alpha u(t) + \beta \int_0^t u(\tau)\, K\,(t,\tau)\, d\tau = \gamma \tag{A-2}$$

when α, β, γ, are constants $K(t,\tau)$ is the kernel function with $t \geq \tau$, and $u(t)$ is the unknown function to be determined.

The defined one dimensional domain Ω, over which the function needs to be approximated, is divided into a finite number (N-1) of subdomains Ω_e i.e.

$$\Omega = \sum_{e=1}^{n=1} \Omega_e, \qquad \Omega_e = (t_{e-1}, t_e) \tag{A-3}$$

Over each subdomain Ω_e, the unknown function $u(t)$ is approximated in the form

$$u_e(t) \simeq U_e(t) = \sum_{i=1}^{2} \phi_i^{(e)}(t)\, U_i^{(e)}, \quad t \in \Omega_e \tag{A-4}$$

where $\phi_i^{(e)}(t)$ are the local linear approximating functions defined by $\phi = N_i \phi_i + N_j \phi_j = [N]\{\phi\}$.

The finite element solution is obtained by using the Galerkin procedure with the integral over the interval (o,t) in equation (A-4) replaced by the sum of the integrals defined over each element. Hence, for the n^{th} element Ω_n, we have

$$\int_{t_{n-1}}^{t_n} \alpha\, \phi_k^{(n)}(t) \sum_{j=1}^{2} \phi_j^{n}(t)\, u_j^{(n)} dt + \beta T_k^{(n)} = \int_{t_{n-1}}^{t} \gamma \phi_k^{(n)}(t) dt \tag{A-5}$$

where

$$T_k^{(n)} = \int_{t_{n-1}}^{t_n} \phi_k^{(n)} \sum_{e=1}^{n-1} \int_{\tau_{e-1}}^{\tau_e} K(x,\tau) \sum_{i=1}^{2} \phi_i^{(e)}\, u_i^{(e)} d\tau \; dt \tag{A-6}$$

Thus equation (A-5) can be re-written as

$$\alpha G_{kj}^{(n)}\, u_j^{(n)} + \beta T_k^{(n)} = \gamma f_k^{(n)}, \qquad k = 1,2 \tag{A-7}$$

where

$$G_{kj}^{(n)} = \int_{t_{n-1}}^{t_n} \phi_k^{(n)}(t)\, \phi_j^{(n)}(t)\, dt$$

$$f_k^{(n)} = \int_{t_{n-1}}^{t_n} \phi_k^{(n)}(t)\, dt$$

The element equations can be combined to yield the global form

$$\alpha[G]\ \{U\} + \beta\ [M]\ \{U\} = \{f\} \qquad \text{(A-8)}$$

where $\{T_k(n)\} = \{M_{ik}^{(n)}\}\ \{U_i\}$

The solution for $\frac{dL}{dt}$ in equation (A-1) is obtained by solving for the model values of u(t) with $\alpha = 3\pi W/8$, $\beta = 2C$, $\gamma = Q/H$, and $K(t,\tau) = 1/(t-\tau)^{1/2}$

Figure A-1 illustrates a comparison between the finite element solution and exact solution (Equation 6) for the indicated reservoir and fracturing fluid flow parameters.

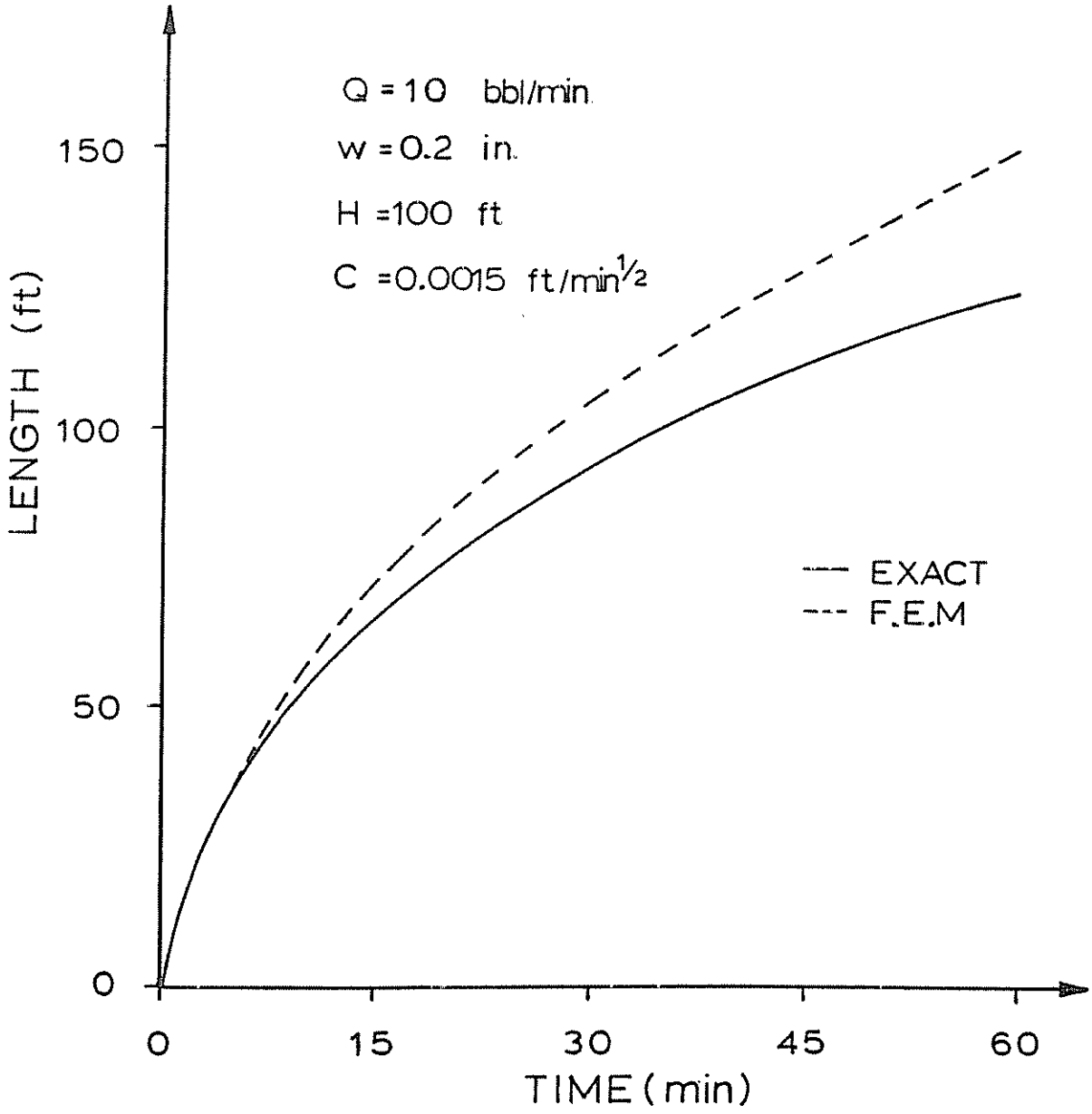

Figure A-1: Length Comparisons Between Analytical and Binite Element Solutions.

APPENDIX B

Two Dimensional and Three Dimensional Stress Intensity Factor Computations

Sophisticated finite element method formulations and numerical evaluations of stress intensity factors for various two and three dimensional crack configurations have been conducted. Selected results are summarized here.

For the two dimensional models, triangular isoparametric singularity elements are used with one side of the original quadrilateral collapsed and the mid side node placed at the quarter points. Figure (B-1) illustrates an inclined crack in a layered medium subjected to in situ and crack pressure loading. A typical mesh plot for this inclined crack model is illustrated in Figure (B-2). Table B-1 reveals the computed stress intensity values for the following cases:

Loading 1 - Vertical loading only

Loading 2 - Horizontal loading in crack pay zone only

Loading 3 - Horizontal loading in adjacent layers only

Loading 4 - Crack pressure loading only

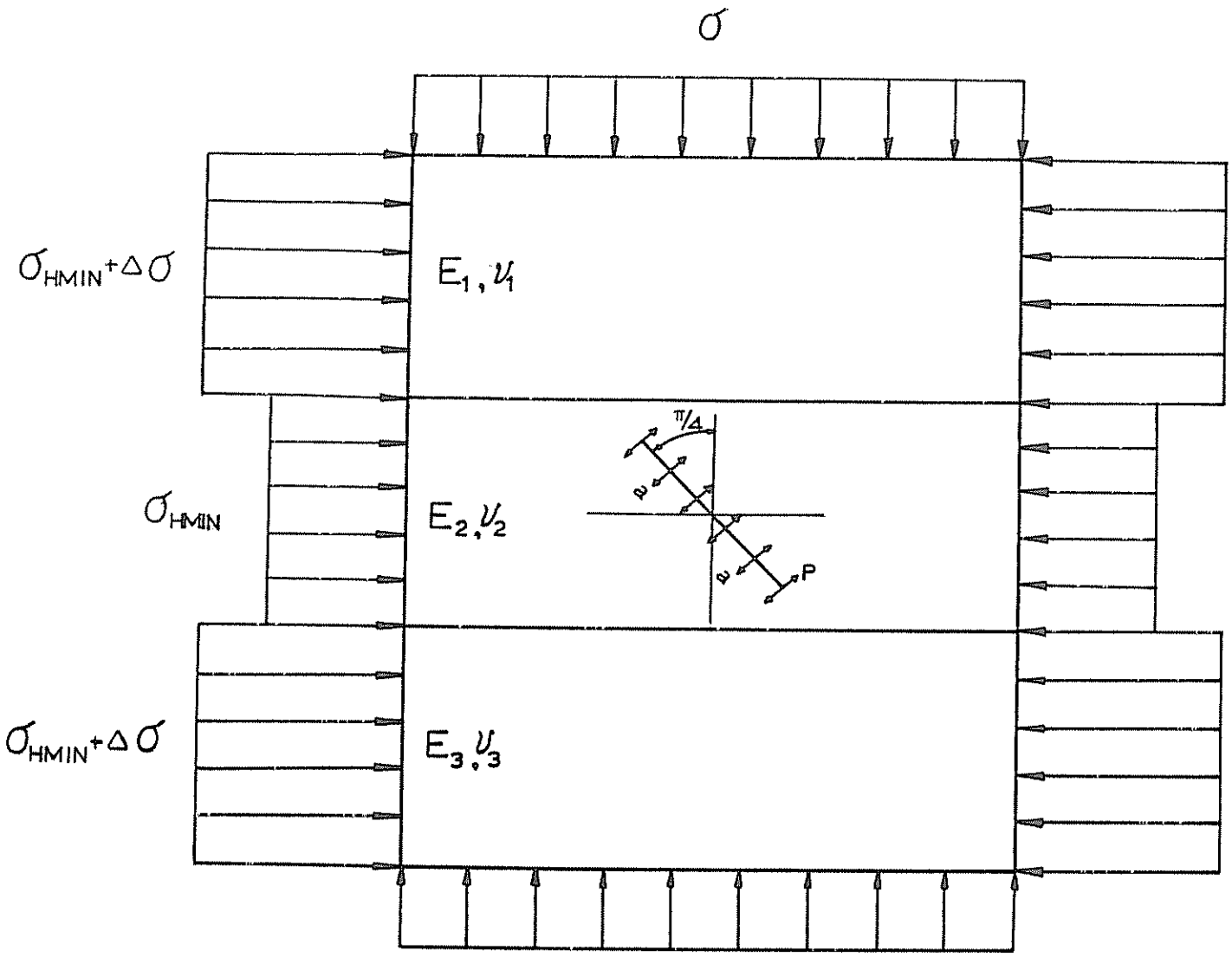

Figure B-1: Inclined Crack Layered Model Subjected to In Situ Crack Pressure Loading.

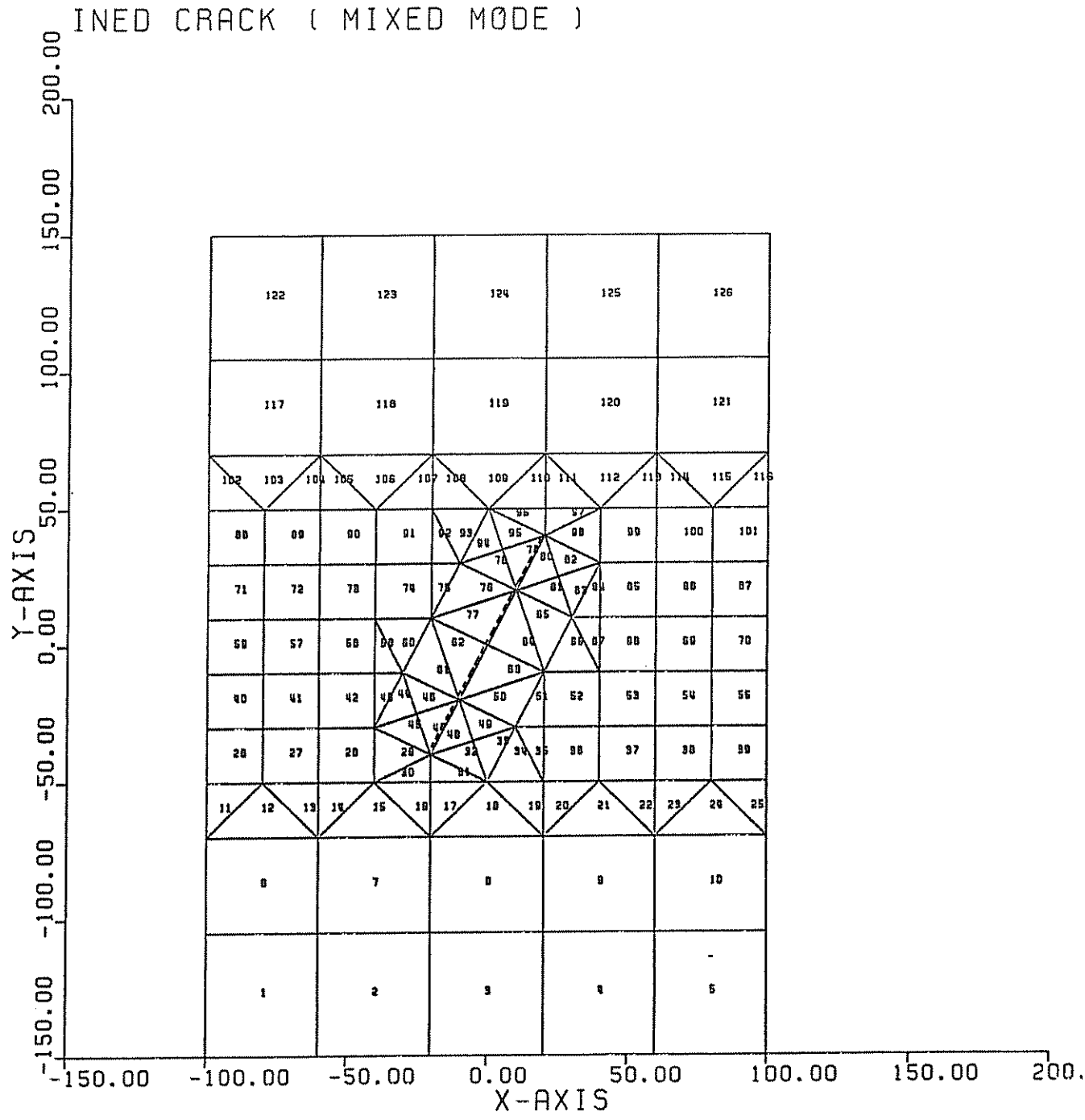

Figure B-2: Finite Element Media for Inclined Crack Model.

Table B-1

Non-dimensionalized Computed Stress Intensity Factors for Inclined Crack (Displacement Method)

Loading Case		1	2	3	4
$\frac{W}{H} = 0.8$ $\frac{a}{W} = \frac{1}{2\sqrt{2}}$ $\frac{E_2}{E_1} = 1.0$	$\frac{K_I}{\sigma\sqrt{a}}$	-1.24	-1.43	-0.27	2.48
	$\frac{K_{II}}{\sigma\sqrt{a}}$	1.02	-1.17	0.18	0.14
$\frac{E_2}{E_1} = 1.25$ INFINITE PLATE	$\frac{K_I}{\sigma\sqrt{a}}$	-1.03	-0.61	-0.33	1.83
	$\frac{K_{II}}{\sigma\sqrt{a}}$	0.90	-0.88	0.05	0.02
$\frac{E_2}{E_1} = 1.00$ INFINITE PLATE	$\frac{K_I}{\sigma\sqrt{a}}$	-1.00			
	$\frac{K_{II}}{\sigma\sqrt{a}}$	0.927			

Stress intensity factors associated with the dendritic fracture model (Figure 16), using the triangular isoparametric element, are given in Table B-2. Stress intensity factors for the joint-vertical crack interaction model (Figure 21) have also been similarly obtained.

The stress intensity factors associated with three dimensional crack models are evaluated by considering twenty node isoparametric quadratic hexahedral elements. The singularity element is obtained by collapsing one face and placing the mid side nodes at the quarter points. Figure B-3 shows an octant of the selected pressurized elliptic crack model. Figures B-4 illustrate typical mesh geometries employed in the computations. The evaluated displacement profiles along the major and minor axes of the elliptical crack are plotted in Figure B-5 along with exact theory comparisons. The variation of the crack opening displacement stress intensity factor along the boundary of the elliptic crack is shown in Figure B-6. Good comparisons between the finite element model and exact theory are evident.

Table B-2

Estimated Stress Intensity Factors for Dendritic Fracture Model

c/b	0.00			0.25			0.50			0.75			1.00		
Loading	P	S_x	S_y	P	S_x	S_y	P	S_x	S_y	P	S_x	S_y	P	S_x	S_y
$K_I^b/(P,S_x,S_y)\sqrt{a}$	0.762	-0.460	-0.320	0.730	-0.465	-0.280	0.672	-0.473	-0.217	0.590	-0.483	-0.120	0.489	-0.488	-0.021
$K_{II}^b/(P,S_x,S_y)\sqrt{a}$	-0.510	-0.030	0.547	-0.392	-0.040	0.630	-0.472	-0.026	0.500	-0.300	-.0130	0.360	-0.248	-0.025	0.257
$K_I^s/(P,S_x,S_y)\sqrt{a}$	-	-	-	1.025	0.210	-1.310	1.471	0.193	-1.681	1.710	0.150	-1.874	1.839	0.107	-1.966

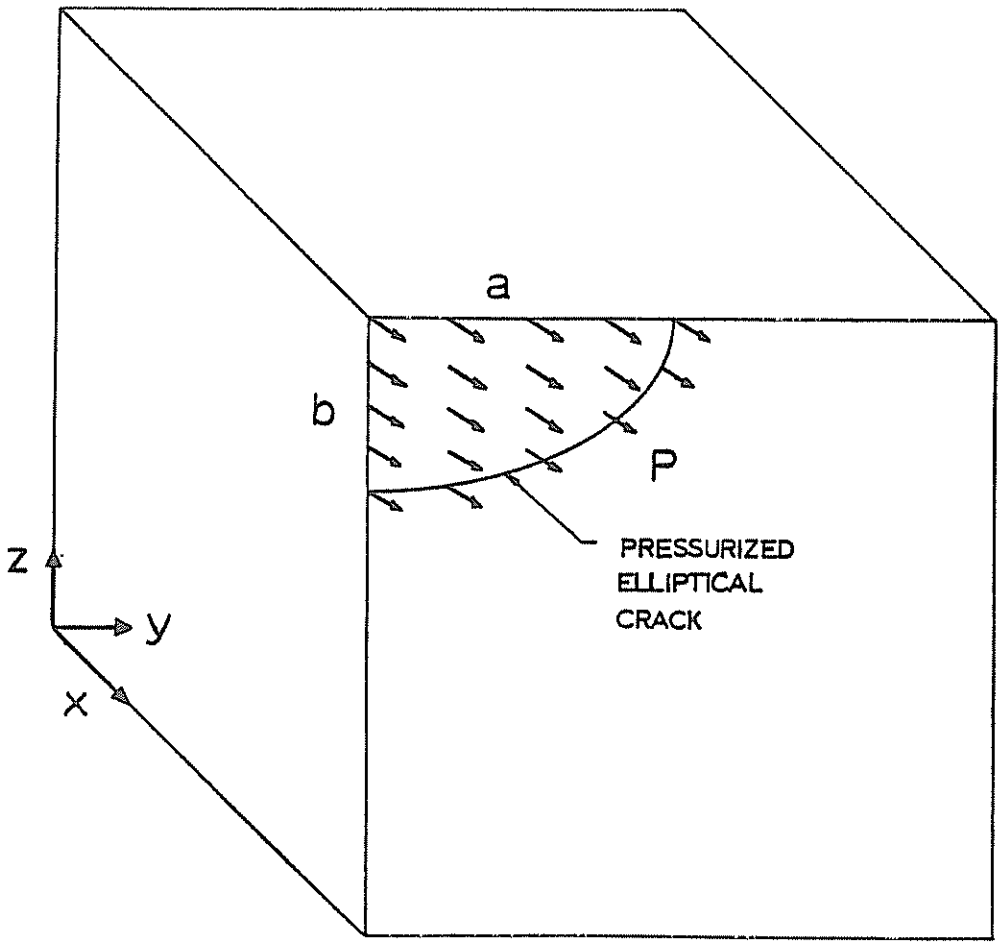

Figure B-3: Pressurized Three Dimensional Elliptical Crack Model.

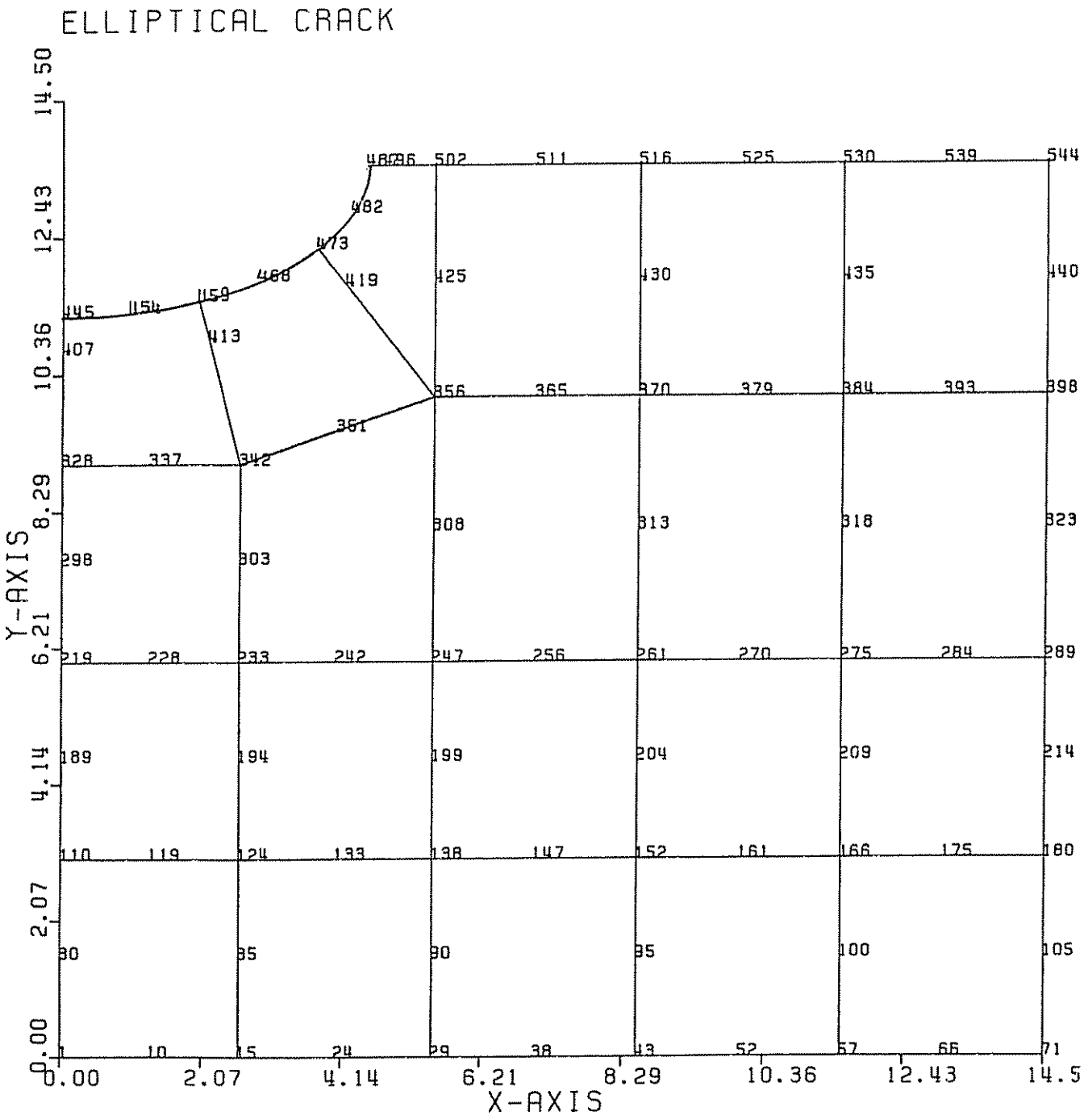

Figure B-4: Selected Mesh for Pressurized Elliptic Crack Model.

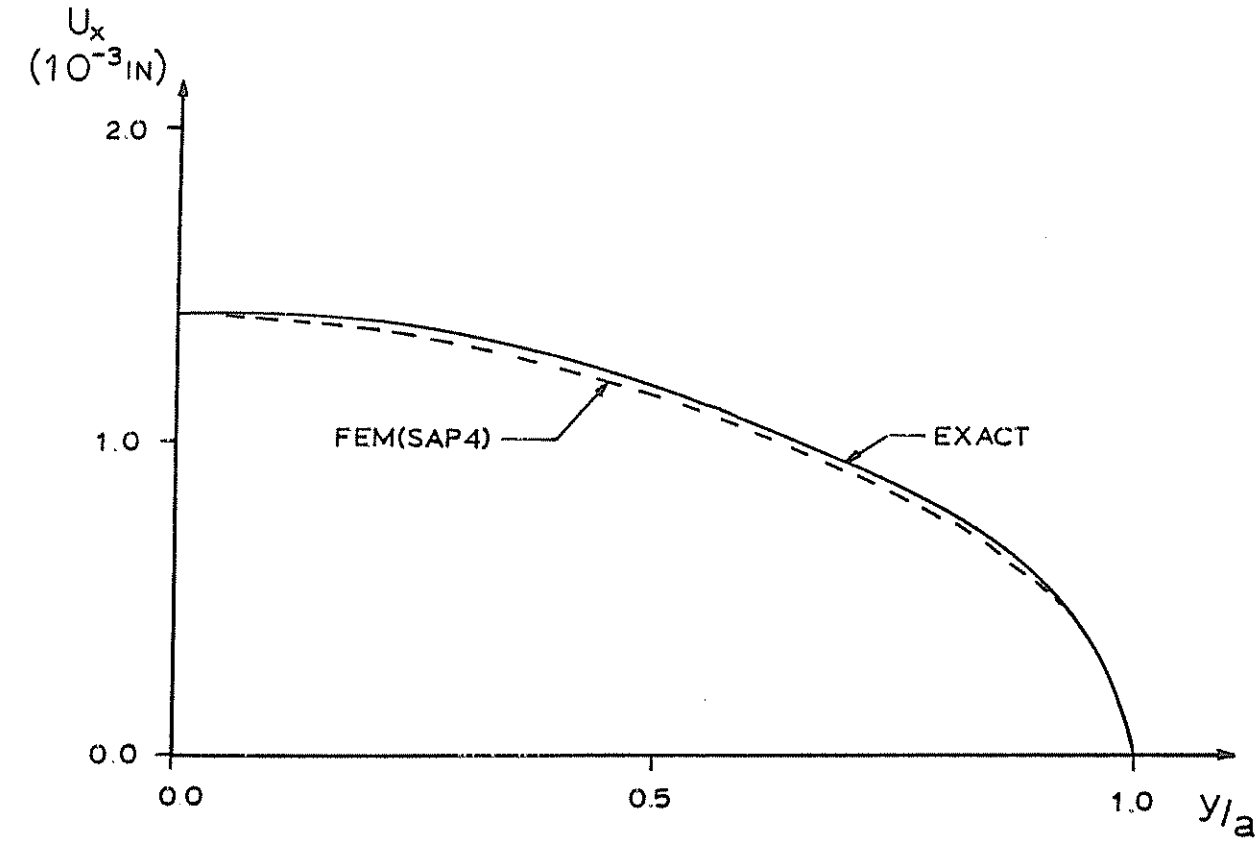

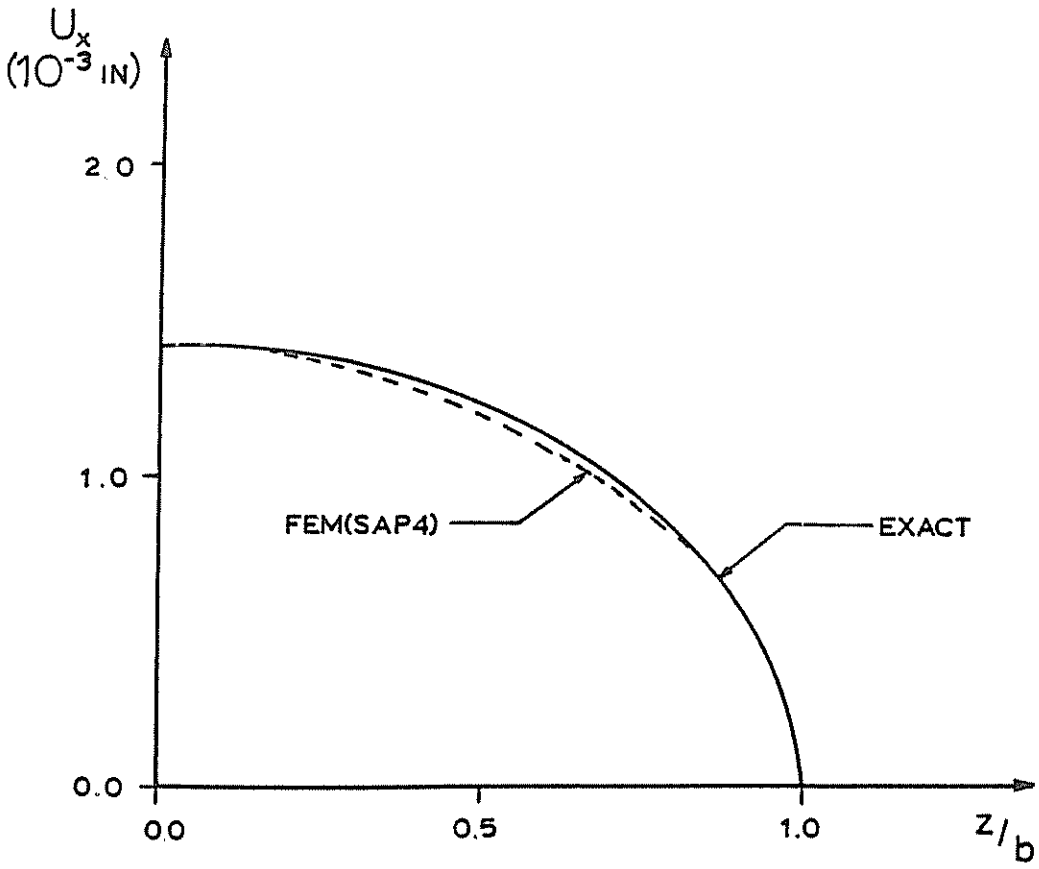

Figure B-5: Elliptic Crack Opening Displacement Profiles.

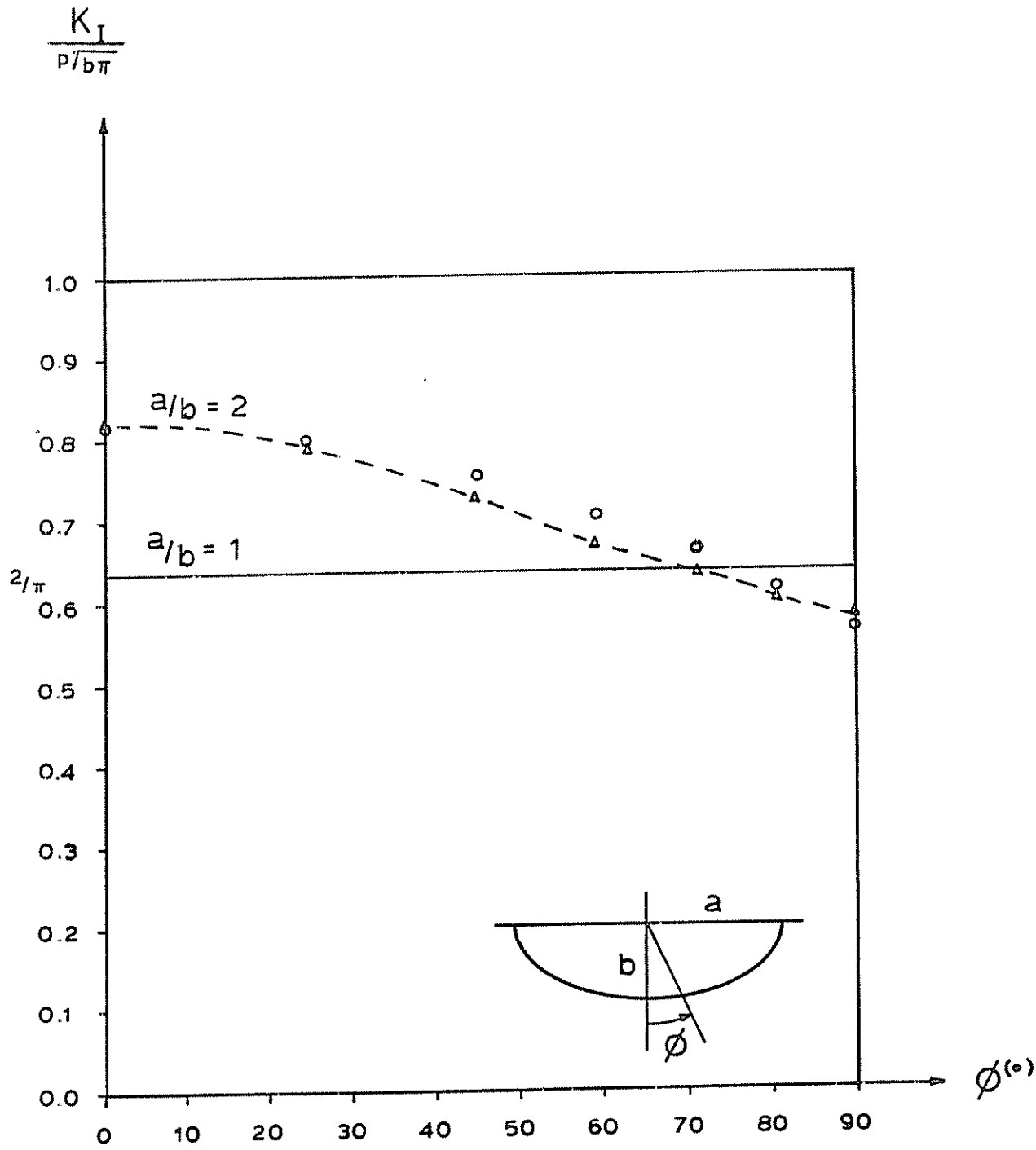

Figure B-6: Comparison of K_I Values for Exact (Δ) and Finite Element Model Solutions.

APPENDIX C

IN SITU STRESS MAGNITUDE COMPUTATIONS
AND FRACTURE GEOMETRY PREDICTIONS

The following table provides an estimate of in situ stress magnitudes and fracture geometry dimensions computed from field data provided by Columbia Gas and Mitchell Energy.

Table C-1

Estimated In Situ Stress Magnitudes and Fracture Geometry Predictions for Selected EGSP Well Sites

Well No.	State	County	σ_{HMIN} psi	σ_{HMAX} psi	σ_{OVBD} psi	Average Width in	Fracture Height ft	Fracture Length ft
20403-1	WV	Lincoln	1637	2611	3668	0.268	173	1260
20403-2	WV	Lincoln	1246	2087	3322	0.258	242	953
20613	OH	Laurence	1268	2193	2163	0.216	203	517
#1-15	MI	Ostego	1024	1638	1463	0.218	72	925
12501-2	WV	Jackson	1646	2831	3695	0.239	70	800
20401-4	WV	Lincoln	901	1780	2523	0.434	116	3240
20401-3	WV	Lincoln	1136	2601	2821	0.329	102	1691
20336-1	WV	Martin	1901	2728	2836	0.282	154	1240
20337-1	WV	Martin	1560	2373	3276	0.360	48	1887
20337-2	WV	Martin	1419	1840	2980	0.328	150	699
1-5	OH	Gallia	1078	1916	2334	0.203	243	408
1-7	OH	Gallia	1499	1879	2508	0.213	194	452
1-8	OH	Gallia	1385	1670	2393	0.163	215	372
1-9	OH	Gallia	1165	1658	2265	0.200	215	419

APPENDIX D

COUPLED ELASTO-DIFFUSIVE RESPONSES ASSOCIATED WITH HYDRAULIC FRACTURING

Hydraulic fracture analysis of a saturated porous rock formation with coupling effects between the matrix deformation and ambient pore fluid diffusion has been conducted by Ruina [14]. This investigation involves the study of the growth of a semi-infinite, plane strain, mode I crack at a constant velocity. The governing field equations, based on the derivations of Rice and Cleary [13], in terms of the stresses σ_{xx}, σ_{xy}, σ_{yy} and the excess pore pressure are

$$\frac{\partial \sigma_{xx}}{\partial x} + \frac{\partial \sigma_{xy}}{\partial y} = 0 \tag{D-1}$$

$$\frac{\partial \sigma_{xy}}{\partial x} + \frac{\partial \sigma_{yy}}{\partial y} = 0 \tag{D-2}$$

$$\left(\frac{\partial^2}{\partial x^2} + \frac{\partial^2}{\partial y^2}\right)\left[\sigma_{xx} + \sigma_{yy} + \frac{3(\nu_u - \nu)}{(1+\nu_u)(1-\nu)} p\right] = 0 \tag{D-3}$$

$$\left[\frac{\partial^2}{\partial x^2} + \frac{\partial^2}{\partial y^2} + \frac{V}{C}\frac{\partial}{\partial x}\right]\left[\sigma_{xx} + \sigma_{yy} + \frac{3}{B(1+\nu_u)} p\right] = 0 \tag{D-4}$$

where $C = 2GkB^2\beta(1+\nu_u)^2/9(\nu_u-\nu)$ is the diffusivity, $\beta = (1-\nu)/(1-\nu_u)$, K is the formation permeability, G is the elastic shear modulus, and B is the ratio of the induced pore pressure to mean hydrostatic compressive stress under undrained conditions. The quantities ν and ν_u denote the drained

and undrained Poisson's ratio, respectively.

The boundary conditions, with reference to Figure D-1 are

$$\frac{\partial p}{\partial y}(x,0) = \sigma_{xy}(x,0) = 0, \quad -\infty < x < \infty$$

$$\frac{\partial \sigma_{xx}}{\partial y}(x,0) = 0 \qquad , \quad 0 < x < \infty \qquad \text{(D-5)}$$

$$\sigma_{yy}(x,0) = -p_f(x) \qquad , \quad -\infty < x < 0$$

and p, σ_{xx}, σ_{yy}, σ_{xy} bounded at infinity. Stress intensity factor solutions to Equations (D-1) through (D-4) with boundary conditions (D-5) for slow, intermediate, and fast crack growth have been presented by Riuna [14]. Two mechanisms of retardation of hydraulic fracture are discussed mathematically. The first mechanism is that the material response in the vicinity of the crack tip displays a softening characteristic (drained). The second mechanism is the decrease of pore pressure in the crack tip with the accompanying decrease in the Terzaghi effective stress.

The above field equations with the associated boundary conditions have been modeled by the finite element approach using an elasto-diffusive code LAMP (Linear Analysis Modular Program) developed at The Ohio State University. Verification of the results obtained by Riuna [14] has been achieved i.e. similar numerical decrease in the K_I stress intensity factor and pore pressure at the crack tip with increasing crack velocity. Various numerical models, with different crack velocities, have also been simulated for Devonian Shale applications. These models demonstrate the connective contribution of the vertical fracture velocity and the pronounced differences in the pore pressure profile and stress intensity

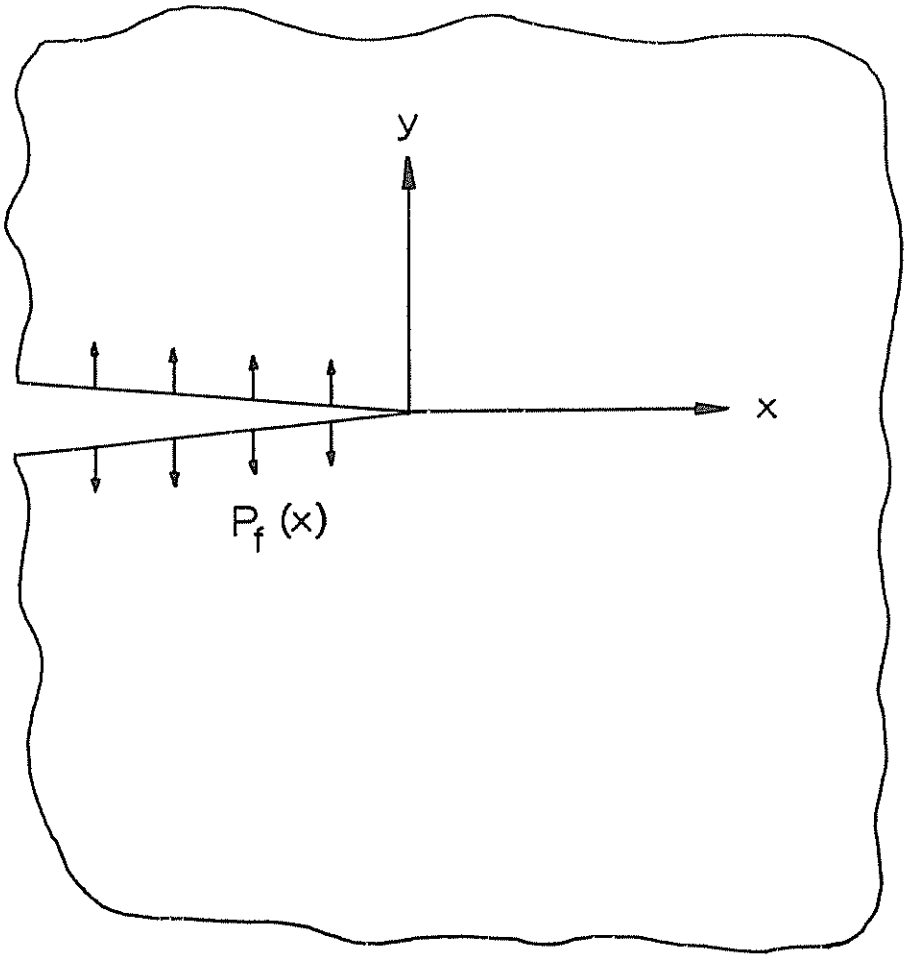

Figure D-1: Semi Infinite Propagating Crack in Infinite Medium.

factor for the various crack velocities. Figure D-2 illustrates the computed stress intensity factor plots for several cases. Follow on studies for optimizing the fracture propagation response in terms of the bottom hole treatment pressure, flow rate, pore pressure, and material properties are recommended.

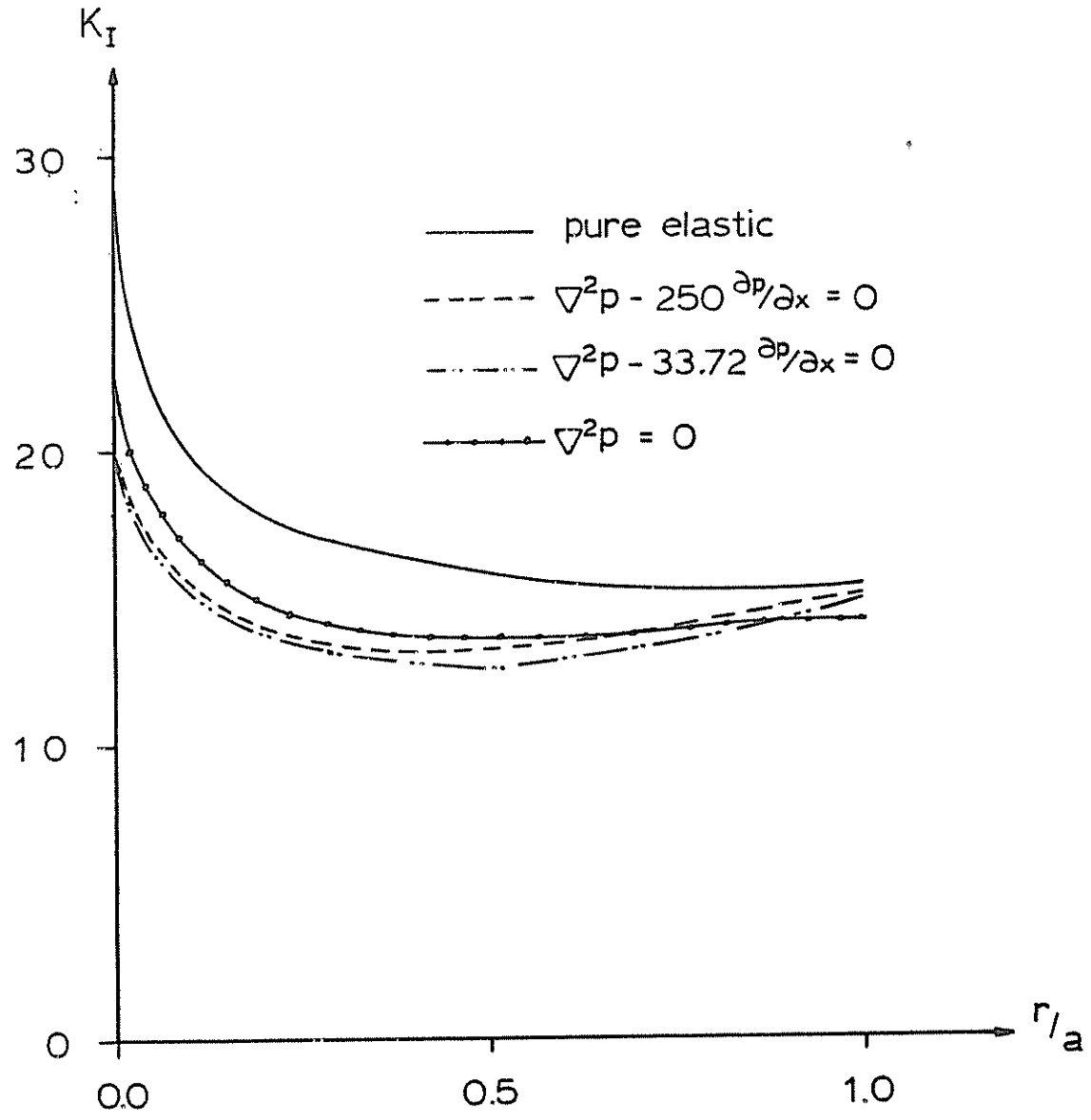

Figure D-2: Crack Opening Stress Intensity Factor for Different Cases in Elasto-Diffusive Medium.

☆ U.S GOVERNMENT PRINTING OFFICE: 1980-740-145/946